



저작자표시-비영리-변경금지 2.0 대한민국

이용자는 아래의 조건을 따르는 경우에 한하여 자유롭게

- 이 저작물을 복제, 배포, 전송, 전시, 공연 및 방송할 수 있습니다.

다음과 같은 조건을 따라야 합니다:



저작자표시. 귀하는 원저작자를 표시하여야 합니다.



비영리. 귀하는 이 저작물을 영리 목적으로 이용할 수 없습니다.



변경금지. 귀하는 이 저작물을 개작, 변형 또는 가공할 수 없습니다.

- 귀하는, 이 저작물의 재이용이나 배포의 경우, 이 저작물에 적용된 이용허락조건을 명확하게 나타내어야 합니다.
- 저작권자로부터 별도의 허가를 받으면 이러한 조건들은 적용되지 않습니다.

저작권법에 따른 이용자의 권리는 위의 내용에 의하여 영향을 받지 않습니다.

이것은 [이용허락규약\(Legal Code\)](#)을 이해하기 쉽게 요약한 것입니다.

[Disclaimer](#)

이학석사 학위논문

황화카드뮴 나노방울의 원자가 전자대 분열 및
광촉매 성능에 관한 연구

**Valence Band Splitting and Photocatalytic
Performances of CdS Nanobubbles**

2014 년 2 월

서울대학교 대학원
화학부 물리화학 전공

김 연 신

A Master's Dissertation

**Valence Band Splitting and Photocatalytic
Performances of CdS Nanobubbles**

By Younshin Kim

Supervisor: Professor Du-Jeon Jang

Major: Physical Chemistry

School of Chemistry

Graduate School of Seoul National University

February 2014

황화카드뮴 나노방울의 원자가 전자대 분열 및
광촉매 성능에 관한 연구

**Valence Band Splitting and Photocatalytic
Performances of CdS Nanobubbles**

지도교수 장 두 전

이 논문을 이학석사 학위논문으로 제출함
2013 년 12 월

서울대학교 대학원
화학부 물리화학 전공

김 연 신

김연신의 이학석사 학위논문을 인준함
2013 년 12 월

위 원 장	_____	강 현 (서명)
부위원장	_____	장 두 전 (서명)
위 원	_____	정 연 준 (서명)

Abstract of Dissertation

A novel fabrication involving silica hard templates and microwave irradiation has been applied to produce hollow CdS nanobubbles with diameters in the submicrometer range but a shell thickness within the quantum confinement regime. The CdS nanobubbles have been found to exhibit unique photophysical properties and exceptional photocatalytic activity.

A brief overview of the topics mentioned in this dissertation is given in Chapter 1. When semiconductor nanoparticles are small enough to be within the quantum confinement regime, their physical and chemical properties differ from those of the bulk materials, examples being changes in melting points, magnetism, optical properties, catalytic properties, and electron densities of states. A general summary of the syntheses methods of nanoparticles and the importance of size and shape tunability is given. Also, the enhancements of the nanoreactor confinement effect for hollow structures in heterogeneous catalysis have been explained.

In Chapter 2, the unique photophysical properties of CdS nanobubbles are discussed. CdS nanobubbles are synthesized with a shell thickness within the quantum confinement range, resulting in valence band splitting. The direct observation of this phenomenon at room temperature has been reported for the first time through a Communication report in the Chemical Communications. The observed data from the photoluminescence spectra have been interpreted by comparison to previous theoretical studies. Discussions on band sensitivity to nanoparticle sizes, magnitudes

of splittings, oscillator strengths of transitions, and estimated relative electron/hole state populations have been given.

Chapter 3 focuses on the fabrication, characterization, and photocatalytic application of CdS nanobubbles. A stepwise synthesis of CdS nanobubbles using silica hard templates and microwave irradiation has been employed to yield well-defined CdS nanobubbles of different sizes. The produced CdS nanobubbles have been completely characterized by transmission electron microscopy, energy dispersive X-ray spectroscopy, high-resolution X-ray diffraction, X-ray photoelectron spectroscopy, and optical spectroscopy. The examination of their photocatalytic activities *via* the degradation of rhodamine B has shown that the pseudo first-order degradation rate constant *via* the nanobubbles is about 20 times larger than that *via* the SiO₂@CdS core@shell nanocomposites due to nanoreactor confinement effect. The enhancement is contributed to the decrease in the activation energy of a new pathway (N-deethylation) and an enhancement of the original pathway (conjugated-ring attack).

Keywords: Cadmium sulfide, Hollow nanospheres, Core@shell nanospheres, Microwave synthesis, Quantum confinement effect, Photocatalysis, Nanoreactor confinement effect

Student Number: 2012-20269

Contents

Abstract of Dissertation	i
List of Figures and Tables	1
Chapter 1. General Introduction	4
1.1. Nanoscale Materials	5
1.2. Valence Band Splitting	11
1.3. Nanostructure Fabrication	15
1.4. Nanoreactor Confinement Effect	19
1.5. References	21
Chapter 2. Direct Observation of Valence Band Splitting Using Room Temperature Photoluminescence of CdS Hollow Submicrospheres	26
2.1. Abstract	27
2.2. Introduction	28
2.3. Experimental Section	29
2.4. Results and Discussion	31
2.5. Conclusion	38
2.6. Acknowledgement	39
2.7. Supporting Information	40

2.8. References	42
Chapter 2. Facile Microwave Fabrication of CdS Nanobubbles with Highly Efficient Photocatalytic Performances	45
3.1. Abstract	46
3.2. Introduction	47
3.3. Experimental Section	50
3.4. Results and Discussion	53
3.5. Conclusion	71
3.6. Acknowledgement	72
3.7. Supporting Information	73
3.8. References	77
Appendices	81
A.1. Stöber Method	81
A.2. Scherrer Equation	82
A.3. Brus Equation	84
A.4. Theoretical Fittings of Line-Scanned EDX Profiles: Core@Shell and Hollow Spheres	85
A.5. List of Publications	88
A.6. List of Presentations	89
Abstract (Korean)	91

List of Figures and Tables

- Figure 1-1.** A simple model depicting the characteristic large surface area of nanomaterials.
- Figure 1-2.** Plots of surface and inner atoms *vs.* nanoparticle diameter (a) and plot of melting point *vs.* nanoparticle diameter of gold.
- Figure 1-3.** Plot of H_c against diameter of ferromagnetic NPs (a). Hysteresis loops showing the variation of magnetization, M , with alternating applied magnetic field of a ferromagnetic NP (b) and a superparamagnetic NP (c); saturation magnetic moment and remnant magnetic moment are represented by M_s and M_r , respectively.
- Figure 1-4.** Schematic illustration of the density of states in metal and semiconductor NPs (a) and the density of states in one band of a semiconductor as a function of dimension (b).
- Figure 1-5.** Fluorescence emission of CdSe@ZnS quantum dots of various sizes exhibiting the quantum confinement effect (left); absorption spectra of gold NPs of various sizes and shapes (right).
- Figure 1-6.** Diagram showing the effects of spin-orbit coupling on the hole states of typical zinc-blende and wurtzite semiconductor NPs.
- Figure 1-7.** Hole energy spectra of $S_{3/2}$ (a), $P_{3/2}$ (b), and $D_{5/2}$ (c) states as a function of μ .
- Figure 1-8.** LaMer diagram describing nucleation and nuclei growth (a) and scheme depicting the growth and stabilization of NPs (b).
- Figure 2-1.** EFTEM images of CdS hollow microspheres H1 (a) and H2 (b) and HRTEM image of H2 (c), with the darkly shaded region representing the shell width. Each thin shell consists of CdS nanocrystallites as marked by dashed circles.

Figure 2-2. Extinction spectra of CdS hollow spheres H1 and H2 (a). $(ah\nu)^2$ plots against $h\nu$ after removal of scattering (c/λ^4 , where c is an arbitrary constant) from the extinction spectra to obtain the band gaps of H1 (b) and H2 (c). The intercept of a dashed line corresponds to the actual CdS band gap while that of a dotted line corresponds to the energy gap created by sulfur-vacancy defects.

Figure 2-3. PL spectra of H1 (a) and H2 (b) suspended in ethanol with excitation at 355 nm. The solid lines correspond to the deconvoluted Gaussian curves and the integrals of Gaussian-fitted curves are shown relatively as vertical lines at the bottom. The exact locations and integrals of the fitted curves are outlined in Table 2-1, and the associated transitions are described in a band-energy diagram (c).

Table 2-1. Peak positions and integrated intensity values of the fitted Gaussian curves in Figure 2-3.

Table 2-2. Relative electron population of $1p_e$ to $1s_e$ (N_{p_e}/N_{s_e}) and relative hole population of $1L_{1/2}$ to $1L_{3/2}$ ($N_{1/2}/N_{3/2}$).

Figure 3-1. Schematic for the synthesis of a CdS nanobubble *via* a hard-template method with the assistance of microwave irradiation.

Figure 3-2. TEM images for the silica nanosphere templates of T300 (a), T370 (b), and T400 (c) and the corresponding CdS nanobubbles of B300 (d), B370 (e), and B400 (f). Each scale bar indicates 200 nm.

Figure 3-3. HRTEM images of CdS nanobubbles B370 at lower (a) and higher (b) magnification. The inset in b shows the FFT pattern of the selected area.

Figure 3-4. Area-normalized EDX elemental profiles of C370 (a) and B370 (b) scanned along the lines in the HAADF images of the insets; symbols indicate experimental data while lines represent theoretical fittings. Elemental mapping profiles of Cd, S, Si, and O for C370 (c) and B370 (d).

- Figure 3-5.** HRXRD spectra of CdS nanostructures B300 (a), B370 (b), and B400 (c), revealing the (111), (220), and (311) lattice planes of the cubic zinc blende CdS crystal structure (reference shown at the bottom, JPCDS Card No. 04-008-8227).
- Figure 3-6.** Complete survey (a), Cd 3d (b), and S 2p (c) XPS spectra of CdS nanobubbles B370. The S 2p_{3/2} and 2p_{1/2} curves have been deconvoluted from Gaussian fitting.
- Figure 3-7.** Baseline-modified absorption spectra of 10 μM RhB solutions in the presence of light without catalysts (a), in the absence of light with 0.1 g L⁻¹ B300 (b), with light and 0.1 g L⁻¹ C300 (c), and with light and 0.1 g L⁻¹ B300 (d), measured at elapsed times indicated in the units of min.
- Figure 3-8.** First-order kinetics, $-\ln(A/A_0)$ vs. t , for the catalytic degradation of 10 μM RhB(aq) *via* B300 CdS nanobubbles at various concentrations indicated in the units of g L⁻¹ (a) and *via* B300, B370, and B400 CdS nanobubbles with varying nanobubble sizes (b) exposed to irradiation by a 300 W Xe lamp. The inset in a shows the variation of $\log k$ with $\log c$ while the inset in b shows the variation of $\log k$ with $\log d$, the outer diameter.
- Figure 3-9.** Proposed mechanisms for the photocatalytic degradation of RhB solutions *via* SiO₂@CdS core@shell composites (a) and CdS nanobubbles (b).
- Table 3-1.** Rate constants (k) for the catalytic degradation of 10 μM RhB solutions *via* CdS nanocatalysts exposed to irradiation by a 300 W Xe lamp.

Chapter 1. General Introduction

1. 1. Nanoscale Materials

Since the term “nanoparticle” (NP) first appeared in the 1980s,¹ interest in the field of nanochemistry has grown exponentially within the last few decades. The number of publications on nanoparticles increased from just 20 publications in the year 1990, to 2,100 publications in 2000, and to 16,000 publications in 2008.² In October 2011, the European Commission defined the term “nanomaterial”:³

“A natural, incidental or manufactured material containing particles, in an unbound state or as an aggregate or as an agglomerate and where, for 50% or more of the particles in the number size distribution, one or more external dimensions is in the size range 1 nm – 100 nm.”

Although the initial interest in nanoscale materials have stemmed from their potential for miniaturizing and developing advanced technologies, the novelty and tunability of the properties of nanomaterials also offer diverse perspectives in interdisciplinary fields.

One of the fundamental characteristics of nanoscale materials is that they have an extremely large surface area-to-mass ratio. As conceptually illustrated in Figure 1-1, the surface area of a cube with an edge length of 1 cm and that of the same volume of cubes with an edge length of 1 nm differ by a factor of 10^7 . This drastic increase in the surface-to-volume ratio influences both the physical and chemical properties of the NP. Figure 1-2a shows that there are a significant number of atoms on the surface of NPs, meaning that properties of the surface atoms will significantly affect, and often

dominate, the overall properties of the nanomaterial. Surface atoms with unsaturated bonding sites or unoccupied coordination sites are weakly bound in comparison to the highly ordered crystallinity of the ‘inner’ atoms, consequently resulting in lower melting points⁴ and higher chemical reactivity for nanomaterials in general (Figure 1-2b).

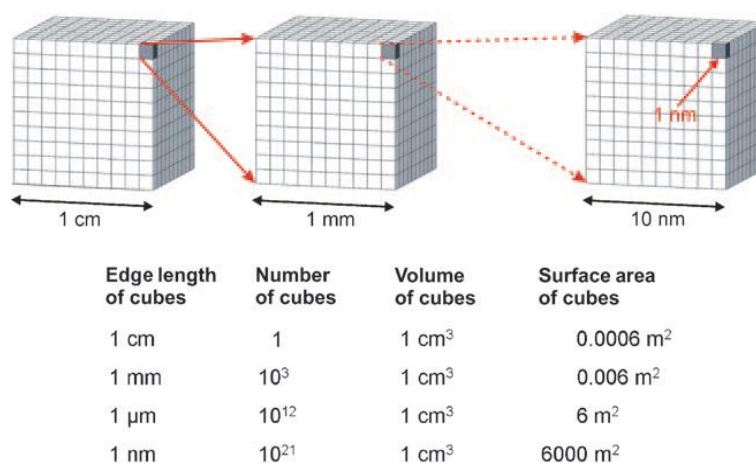


Figure 1-1. A simple model depicting the characteristic large surface area of nanomaterials (reproduced from ref.²).

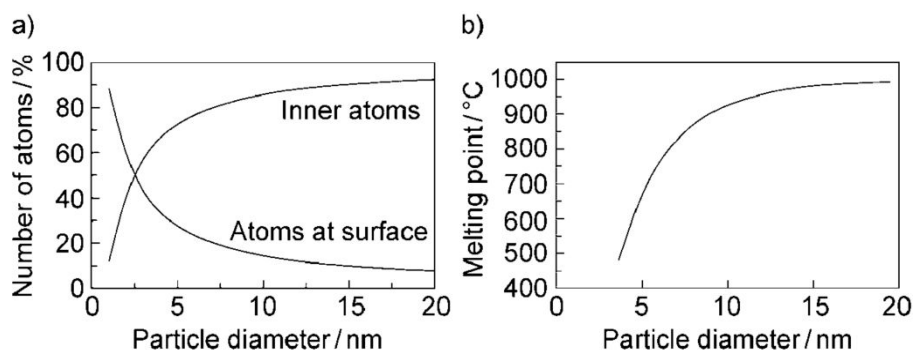


Figure 1-2. Plots of surface and inner atoms vs. nanoparticle diameter (a) and plot of melting point vs. nanoparticle diameter of gold NPs (reproduced from ref.²).

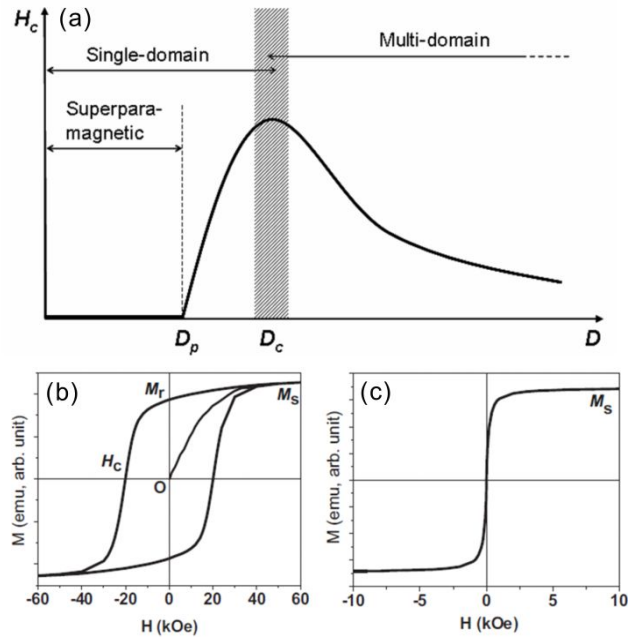


Figure 1-3. Plot of H_c against diameter of ferromagnetic NPs (a). Hysteresis loops showing the variation of magnetization, M , with alternating applied magnetic field of a ferromagnetic NP (b) and a superparamagnetic NP (c); saturation magnetic moment and remnant magnetic moment are represented by M_s and M_r , respectively (modified reproduction of ref.⁹⁻¹⁰).

Nanoscale materials also show a change in magnetic properties in comparison to their bulk counterparts. The domain theory states that a ferromagnetic material, at temperatures below the Curie temperature, will spontaneously divide into smaller magnetic domains in order to reduce the magnetostatic energy.⁵ However, when the NP size is smaller a certain critical diameter, D_c , the domain theory fails to apply and the NP exists as a single domain because the domain wall energy surpasses the stabilization energy of a multi-domain structure (Figure 1-3a). When the size of the NP decreases even further to a diameter, D_p , the nanoscale material now becomes

superparamagnetic, and this phenomena can be explained by the equation for the relaxation of the magnetization organization orientation of each particle:⁶

$$T_B = \frac{KV}{k_B \ln(\frac{\tau_m}{\tau_0})} \quad (1-1)$$

where T_B =blocking temperature, K = magnetic anisotropy constant, V = volume of the NP, k_B = Boltzmann constant, τ_m = measurement time, and τ_0 = attempt period ($\sim 10^{-9}$ – 10^{-10}). At NP sizes below D_p , the volume of the NP becomes so small that KV , the energy barrier for magnetization to flip in a ferromagnetic material is comparable to $k_B T$, the thermal energy. Thus, magnetization is subjected to random thermal fluctuations such that the ferromagnetic alignment flips up and down faster than the measurement time, and the NP seems to exhibit a paramagnetic-like behavior, hence called superparamagnetism. For ferromagnetic NPs of a specified volume, the minimum temperature for superparamagnetism to occur is the blocking temperature, T_B .⁷ Scientists have focused much attention into controlling the sizes of magnetic NPs for optimization in a variety of applications. Ferromagnetic NPs with a size along the borderline size for single- and multi-domain structures, D_c , show the highest coercivity, H_c , which is key to high-density data storage media (Figure 1-3b).⁷ Superparamagnetic NPs with extremely low T_B show higher magnetic susceptibility than paramagnetic materials, showing high potential for applications in biomedicine (Figure 1-3c).⁸

Nanoscale materials also show unique optoelectrical properties as a result of their small size. When one or more of the dimensions of a semiconductor NP becomes comparable to the Bohr exciton radius, a_B , the NP exhibits a phenomenon referred to as the quantum confinement effect. The band-like nature of the valence electronic

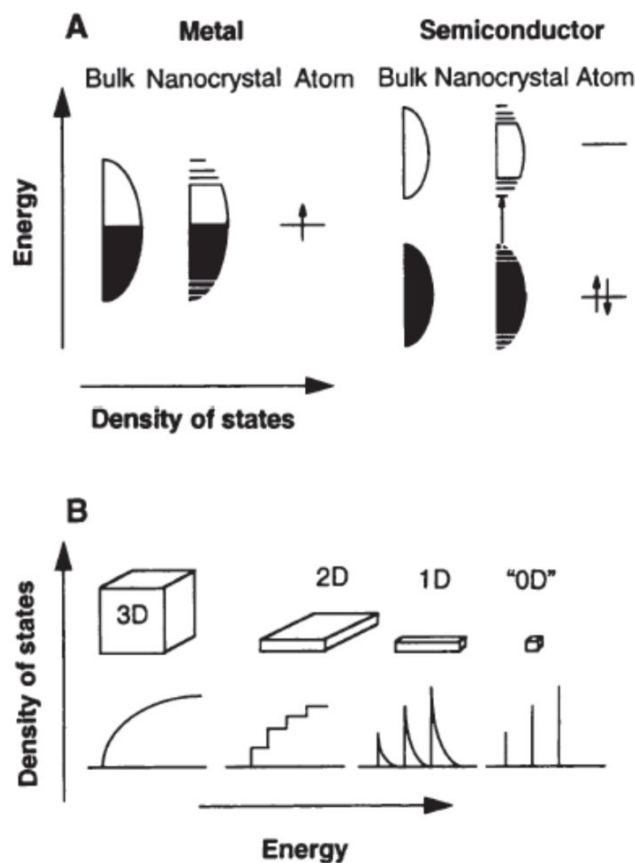


Figure 1-4. Schematic illustration of the density of states in metal and semiconductor NPs (a) and the density of states in one band of a semiconductor as a function of dimension (b); (reproduced from ref.⁴).

states diminishes, meaning that the absorption peak maximum is blue-shifted and that the band-gap energy is increased (Figure 1-4a; for further details, see section 1.2).¹¹⁻¹² For metals, because the Fermi level is in the middle of the conduction band, the quantum confinement effect does not affect its optical properties as obviously. However, metal NPs exhibit changes in the absorption band due to another phenomenon called surface plasmon resonance (SPR).¹³⁻¹⁵ In metal NPs, the mean free path of free electrons is greater than at least one dimension, resulting in a high

density of electrons at the surfaces. When light is irradiated, the polarized electron density oscillates in resonance with the frequency of the irradiated light, ultimately causing a standing surface plasmon oscillation.¹⁶ SPR is dependent on the size and shape¹⁵ of the metal NP and also the dielectric constants of the metal NP and its surrounds. Figure 1-5 summarizes the photophysical properties observed for both semiconductor and metal NPs.

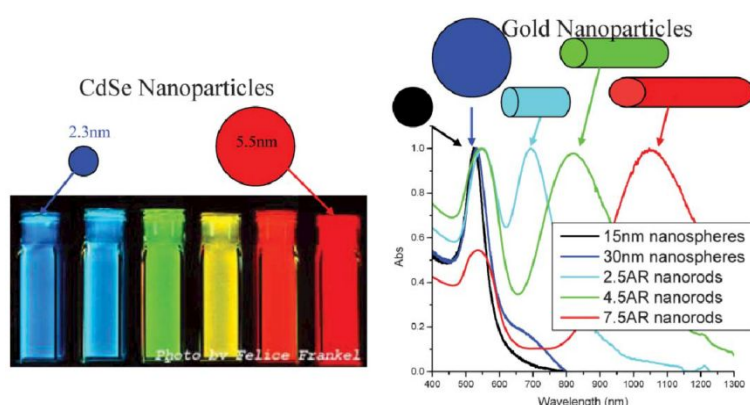


Figure 1-5. Fluorescence emission of CdSe@ZnS quantum dots of various sizes exhibiting the quantum confinement effect (left); absorption spectra of gold NPs of various sizes and shapes (right); (reproduced from ref.¹⁴).

Nanoscale materials have also been reported¹⁷⁻²³ to be excellent catalysts due to their enlarged surface area per volume, enhanced catalytic reactivity of the surface atoms, and the shape of the nanoparticles. The enlarged surface area-to-volume ratio obviously correlates directly to an increase in the number of catalytically active defect sites, and depending on the NP, the surface of the NP may be catalytically more active than the surface of its bulk counterpart (see section 1.4).

At the nanoscale, physical properties such as the surface-to-volume ratio, melting point, magnetism, and optical properties, as well as chemical properties such as reactivity and catalytic efficiency, can be controlled. Research at the nanoscale continues to expand because the tunable properties of nanoscale materials make them limitless prospects for applications in interdisciplinary fields of science.²⁴

1.2. Valence Band Splitting

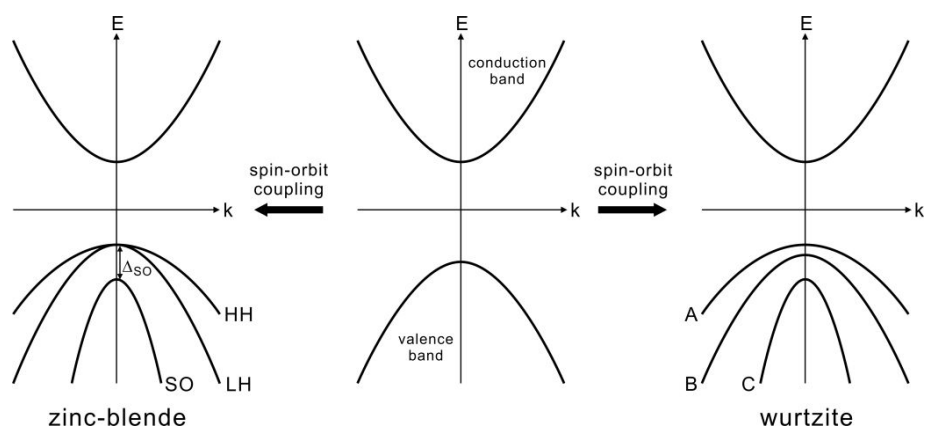


Figure 1-6. Diagram showing the effects of spin-orbit coupling on the hole states of typical zinc-blende and wurtzite semiconductor NPs.

In order to take full advantage of the unique optical and electrical properties of semiconductor NPs mentioned section 1.1, it is important to completely understand their band structures. The electronic structure of II-VI and III-VI semiconductor NPs

have been extensively modelled by the tight-binding (TB) model and the effective mass approximation (EMA).²⁵ The TB model is an atomistic model based on similar principles to those of the linear combination of atomic orbitals (LCAO) method, where the electrons are assumed to be ‘tightly bound’ to each isolated atom. The TB method is more suited for calculating the exact electronic structure of a single surface atom or a very small cluster of atoms.²⁶ The EMA, on the other hand, is a continuum model based on $\mathbf{k}\cdot\mathbf{p}$ perturbation theory and envelope function approximations. It is based on the idea that an electron in a crystal has an effective mass when compared to the mass of a free electron. The EMA allows for simple labelling of electronic densities of states according to global symmetries.²⁷⁻²⁸

For most II-VI and III-V semiconductor materials, the one-band model of EMA shows that the conduction band is primarily formed from s -orbitals of the metal cation and the valence band mainly resembles the p -orbitals of the anion. Although the conduction band can be approximated by simple parabolic bands, the valence band is highly stressed by nonparabolicity. When spin-orbit interactions are taken into consideration, the valence band splits into degenerate bands for both zinc-blende and wurtzite structures as shown in Figure 1-6. In the zinc-blende crystal lattice, the spin-orbit split-off energy, Δ_{SO} , splits the 6-fold degenerate valence band into 2 different valence bands: a 4-fold degenerate band corresponding to total angular momentum $J = 3/2$ and a 2-fold degenerate band corresponding to $J = 1/2$. For $J = 3/2$, the $m_J = \pm 3/2$ subband is referred to as the heavy-hole (HH) band and the $m_J = \pm 1/2$ subband is referred to as the light-hole (LH) band. For $J = 1/2$ and $m_J = \pm 1/2$, the subband is referred to as the spin-orbit split-off (SO) band. In wurtzite crystals, the degeneracy of

the uppermost valence bands is removed by crystal-field splitting; the three valence bands are labeled A-, B-, and C-subband. The following discussions will be based on the EMA of zinc-blende structures.

At $k = 0$, where k is the wave vector reduced to the first Brillouin zone, the degeneracies of these subbands will not be lifted unless the NP experiences strong anisotropic effects and/or is within the strong confinement regime of ~ 2 exciton Bohr radii.²⁹⁻³⁰ When strong confinement-induced valence band mixing occurs, the degeneracy is further lifted and the hole wavefunctions become linear combinations of the different valence band states with mixed s - d -type symmetry. The studies conducted in this thesis are based on the valence band splitting of cubic zinc-blende CdS nanobubbles (Chapter 2).

From the development of the Kane model³¹ in 1957, several important progressions to the quantum mechanical approach to valence band splitting have been generally accepted. In the Hamiltonian describing hole masses, deviations from the parabolic model have been accounted for by the Luttinger parameters,³² γ_1 , γ_2 , and γ_3 . Specific alterations to the kinetic energy term of the hole, $\hat{\mathbf{H}}_h$ as described by eq. 1-3, in the Hamiltonian operator, $\hat{\mathbf{H}}$ as described by eq. 1-2, have been developed.³³⁻³⁶

$$\hat{\mathbf{H}} = -\frac{\hbar^2 \nabla_e^2}{2m_e} + \hat{\mathbf{H}}_h - \frac{e^2}{\epsilon|r_e-r_h|} + V_e(r_e) + V_h(r_h) \quad (1-2)$$

$$\begin{aligned} \hat{\mathbf{H}}_h = \hat{\mathbf{H}}_{LU} = & \left(\gamma_1 + \frac{5}{2}\gamma_2 \right) \frac{\hat{\mathbf{p}}^2}{2m_0} - \frac{\gamma_2}{m_0} (p_x^2 J_x^2 + p_y^2 J_y^2 + p_z^2 J_z^2) \\ & - \frac{2\gamma_3}{m_0} [\{p_x p_y\}\{J_x J_y\} + \{p_y p_z\}\{J_y J_z\} + \{p_z p_x\}\{J_z J_x\}] \end{aligned} \quad (1-3)$$

where \hbar is the reduced Planck constant, ∇_e^2 is the Laplace operator, m_e is the effective electron mass, e is the elementary charge, ϵ is the dielectric constant of the material, r_e

is the electron radius, r_h is the hole radius, $V_e(r_e)$ is the potential energy of the electron as a function of r_e , $V_h(r_h)$ is the potential energy of the electron as a function of r_h , m_0 is the free electron mass, $\hat{\mathbf{p}}$ is the hole momentum operator, and J is the 3/2-angular momentum operator. In eq. 1-2, the first term represents the kinetic energy of the electron, the second term represents the kinetic energy term of the hole (eq. 1-3), the third term represents the electron-hole Coulomb attraction, the fourth term represents the potential energy of the electron, and the fifth term represents the potential energy of the hole.

By restricting the shape of the NP to spherical symmetry, the above-mentioned equations have been simplified to the Baldereschi-Lipari³⁷ Hamiltonian, $\hat{\mathbf{H}}_{BL}$:

$$\hat{\mathbf{H}}_h = \hat{\mathbf{H}}_{BL} = \frac{\gamma_1}{2m_0} \left[\hat{\mathbf{p}}^2 - \frac{\mu}{9} (\mathbf{p}^{(2)} \mathbf{J}^{(2)}) \right] \quad (1-4)$$

where $\mathbf{p}^{(2)}$ and $\mathbf{J}^{(2)}$ are second-rank tensor operators and the coupling parameter, μ , is defined by:

$$\mu = \frac{6\gamma_3 + 4\gamma_2}{5\gamma_1} \quad (1-5)$$

The Hamiltonian was further simplified by Xia³⁸ in 1989 by assuming a small band warping such that $\gamma_2 = \gamma_3$ in a spherical quantum well with an infinite potential barrier. This simplifies the coupling parameter to:

$$\mu = \frac{2\gamma_2}{\gamma_1} \quad (1-6)$$

By doing so, Xia has reported that hole states do not vary monotonically with μ , which describes the level of spin-orbit interaction, due to the mixing of HH and LH states (Figure 1-7). The resulting states with s - d -type symmetry are now linear combinations

of different valence band states.³⁹ Experimental evidence for valence band splitting in CdS nanobubbles has been interpreted in Chapter 2 of this thesis.⁴⁰

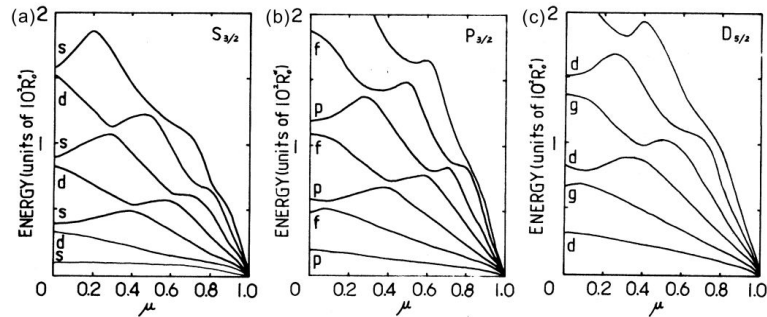


Figure 1-7. Hole energy spectra of $S_{3/2}$ (a), $P_{3/2}$ (b), and $D_{5/2}$ (c) states as a function of μ (modified reproduction of ref.³⁸).

1.3. Nanostructure Fabrication

Seeing as nanoscale materials are extremely sensitive to size, it is important to be able to synthesize and control the fabrication of monodisperse NPs with small size distributions. The most widely accepted synthesis of small nanospheres is the hot-injection method,⁴¹⁻⁴² which involves the rapid injection of precursors into a hot coordinating solvent. The formation of NPs can be described by the LaMer diagram⁴³ in Figure 1-8a. In stage I, otherwise referred to as the prenucleation stage, monomer build-up in the solution surpasses supersaturation ($S > 1$) but precipitation does not occur due to the high energy barrier for spontaneous homogeneous nucleation. In stage II, otherwise known as the nucleation stage, supersaturation reaches critical

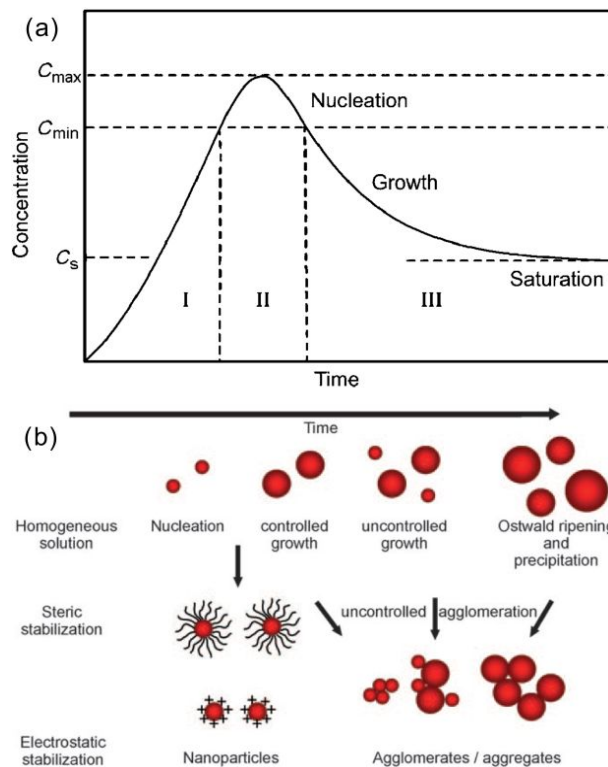


Figure 1-8. LaMer diagram describing nucleation and nuclei growth (a) and scheme depicting the growth and stabilization of NPs (b) (modified reproduction of ref.^{2,43}).

supersaturation, S_c , such that the supersaturation is now high enough to overcome the energy barrier for nucleation. At this stage, stable nuclei are formed in a very short period of time. In stage III, or else the growth stage, nucleation in the preceding stage causes an exhaustion of monomers to a supersaturation below S_c , ceasing all nucleation. The particles now keep growing at a slower rate as long as the solution is supersaturated ($S > 1$). When supersaturation is still much greater than 1 ($S \gg 1$), growth of the NPs is controlled by diffusion such that the radii of smaller NPs grows at a faster rate than the radii of larger NPs. For diffusion-controlled growth, variance of the size distribution is reduced and this stage is referred to as the size focusing regime.

However, as supersaturation decreases, the precipitation rate becomes faster than the diffusion rate, such that the atoms on the surfaces of the smaller NPs diffuse back into solution and precipitate onto the surfaces of the more stable larger NPs. At this stage, variance of the size distribution increases and this stage is called the size defocusing regime; this process is also referred to as Ostwald ripening.⁴⁴⁻⁴⁵ Overall, burst nucleation and control of the growth process allows for the fabrication of uniform spherical NPs.^{2,4,46}

In 2001, burst nucleation was achieved by a much simpler synthesis called the heat-up method,⁴⁷⁻⁴⁹ a simple batch process in which the precursors are mixed into the surfactant solution at lower temperature and then heated up to a specific temperature. Reaction kinetics of the heat-up process has been found to also follow stages II and III of the LaMer diagram, allowing for homogeneous nucleation. It is important to note that because the surfaces of NPs are so reactive, they must be stabilized by means such as steric stabilization, achieved by surfactants or polymers, or electrostatic stabilization, achieved by the adsorption of ions on the NP surfaces (Figure 1-8b). Otherwise, stabilization may be attained by fabrication of composite structures such as core@shell structures or the attachment of NPs onto a substrate or template. Another way to overcome stability issues is to design nanostructures which are not in the nanoscale in all three dimensions. An example is given by the CdS nanobubbles synthesized in this thesis. Despite the very thin shell thickness of 11 nm, the overall diameter of the nanobubbles ranges from 300 to 400 nm.

Currently, a wide diversity of methods besides the hot-injection and heat-up methods are being utilized in the syntheses of nanoscale materials, examples being but

not limited to hydro/solvothermal,⁵⁰ electrochemical, laser-induced⁵¹ fabrication methods. In particular, the microwave method has been gaining popularity and has been adopted in our fabrication process. By using microwave irradiation, heat is not transferred from the container walls as it is in conventional heating, which results in temperature fluctuations throughout the solution; instead, irradiation, and hence heat, is homogeneously induced throughout the solution such that nucleation also occurs homogeneously.⁵²⁻⁵⁴

Depending on the design of the target nanoscale material for fabrication, different syntheses must be used. Among these designs, hollow-structured nanomaterials are gaining current interest for potential application as chemical reactors,⁵⁵ drug delivery carriers,⁵⁶ energy-storage devices⁵⁷⁻⁵⁸ and efficient catalysts⁵⁹ due to their distinct characteristics specified by tunable features such as shell thickness and interior cavity size. The main methods of syntheses of hollow structures are *via* hard template,⁶⁰ soft template,⁶¹⁻⁶² and template-free⁶³ methods. The hard-template method involves the initial application of a solid hard template such as polystyrene and SiO₂ onto which a shell is coated. Then, the initial hard template is etched out. This method allows for the most control in size and shape, but the downsides are that it requires many steps and that it is limited by surface functionalization of the hard templates. This soft-template method utilizes malleable liquid or gas templates. It may require fewer steps than the hard-template method but the soft-template method is usually limited to spherical shape and it is difficult to create soft templates with high size uniformity. The template-free method takes advantage of the Kirkendall effect,⁶³ which forms pores due to the difference in diffusion rates between two components in

a diffusion couple. The template-free method typically requires the least number of steps, but also has the least number of synthetic variables that can be controlled. The hard-template method has been used, as well as the microwave irradiation, for the synthesis of CdS nanobubbles.

1.4. Nanoreactor Confinement Effect

As previously mentioned, the chemical reactivity of NPs may be modified by their size and shape. The catalytic activities of NPs have been reported to change immensely with changes in shape of the NPs. Extensive studies⁶⁴ on colloidal metallic nanocatalysts with different shapes show that NPs with sharp edges, sharp corners, or rough surfaces due to an increase in the number of surface atoms that are not fully coordinated, which are more reactive towards catalysis. Examples include multiarmed Pt nanostars⁶⁵ and multioctahedral Pt nanocrystals.⁶⁶

Another shape that is known to largely enhance catalytic efficiency is hollow nanostructures. A portion of this enhancement is owed to the dramatic increase in the surface-to-volume ratio; the volume is decreased and the surface area is increased for a hollow NP in comparison to its counter filled solid NP. However, hollow-structured nanocatalysts have been found to possess another

form of enhancement besides that caused by an increased surface-to-volume ratio. This enhancement is referred to as the nanoreactor confinement effect, or the nanocage effect.

Experiments by Mahmoud⁶⁷ *et al.* have indicated that photocatalysis in highly photocatalytic Pd and Pt hollow nanocubes occurs in the inner cavities of the hollow structures. Kwak⁶⁸ *et al.* have shown that filled Pt core@shell nanospheres require a higher activation energy in comparison to the corresponding hollow Pt nanospheres. These findings lead to suggest that the inner surfaces have active sites which are more catalytically active than those on the outer surfaces. This may occur due to the inner surface being not as well capped as the outer surfaces. Otherwise, the cage-like structure of the nanoreactor may increase the steady-state concentration of the species involved in the rate-determining step. Build-up of these intermediate species within the nanocavity may speed up the catalytic process.⁶⁹ The CdS nanobubbles studied in this thesis also exhibit the nanocage effect (see Chapter 3).

1.5. References

- (1) A. Henglein, *Chem. Rev.* **1989**, *89*, 1861-1873.
- (2) H. Goesmann, C. Feldmann, *Angew. Chem. Int. Ed.* **2010**, *49*, 1362-1395.
- (3) in *Official Journal of the European Union, Vol. L 275*, European Commission, **2011**, pp. 38-40.
- (4) A. P. Alivisatos, *Science* **1996**, *271*, 933-937.
- (5) H. Gleiter, *Adv. Mater.* **1992**, *4*, 474-481.
- (6) A.-H. Lu, E. L. Salabas, F. Schüth, *Angew. Chem. Int. Ed.* **2007**, *46*, 1222-1244.
- (7) J. Park, K. An, Y. Hwang, J.-G. Park, H.-J. Noh, J.-Y. Kim, J.-H. Park, N.-M. Hwang, T. Hyeon, *Nat Mater* **2004**, *3*, 891-895.
- (8) D. Kim, N. Lee, M. Park, B. H. Kim, K. An, T. Hyeon, *J. Am. Chem. Soc.* **2008**, *131*, 454-455.
- (9) B. D. Cullity, Addison-Wesley, Reading, MA, **1972**.
- (10) S. Sun, *Adv. Mater.* **2006**, *18*, 393-403.
- (11) J. Lee, V. C. Sundar, J. R. Heine, M. G. Bawendi, K. F. Jensen, *Adv. Mater.* **2000**, *12*, 1102-1105.
- (12) C. B. Murray, D. J. Norris, M. G. Bawendi, *J. Am. Chem. Soc.* **1993**, *115*, 8706-8715.
- (13) Z. Liu, W. Hou, P. Pavaskar, M. Aykol, S. B. Cronin, *Nano Lett.* **2011**, *11*, 1111-1116.
- (14) S. Eustis, M. A. El-Sayed, *Chem. Soc. Rev.* **2006**, *35*, 209-217.

- (15) Q. Zhang, J. Ge, T. Pham, J. Goebel, Y. Hu, Z. Lu, Y. Yin, *Angew. Chem. Int. Ed.* **2009**, *48*, 3516-3519.
- (16) Y. Gong, Y. Zhou, L. He, B. Xie, F. Song, M. Han, G. Wang, *Eur. Phys. J. D* **2013**, *67*, 1-6.
- (17) A. J. Gellman, N. Shukla, *Nat Mater* **2009**, *8*, 87-88.
- (18) V. Polshettiwar, R. S. Varma, *Green Chemistry* **2010**, *12*, 743-754.
- (19) S. H. S. Chan, T. Yeong Wu, J. C. Juan, C. Y. Teh, *J. Chem. Technol. Biotechnol.* **2011**, *86*, 1130-1158.
- (20) U. I. Gaya, A. H. Abdullah, *J. Photochem. Photobiol., C* **2008**, *9*, 1-12.
- (21) H. Zhou, Y. Qu, T. Zeid, X. Duan, *Energy Environ. Sci.* **2012**, *5*, 6732-6743.
- (22) A. Z. Moshfegh, *J. Phys. D: Appl. Phys.* **2009**, *42*, 233001.
- (23) H. Kisch, *Angew. Chem. Int. Ed.* **2013**, *52*, 812-847.
- (24) D. V. Talapin, J.-S. Lee, M. V. Kovalenko, E. V. Shevchenko, *Chem. Rev.* **2009**, *110*, 389-458.
- (25) J. G. Díaz, J. Planelles, G. W. Bryant, J. Aizpurua, *J. Phys. Chem. B* **2004**, *108*, 17800-17804.
- (26) J. G. Díaz, M. Zieliński, W. Jaskólski, G. W. Bryant, *Physical Review B* **2006**, *74*, 205309.
- (27) D. O. Demchenko, L.-W. Wang, *Physical Review B* **2006**, *73*, 155326.
- (28) P. Horodyská, P. Němec, D. Sprinzl, P. Malý, V. N. Gladilin, J. T. Devreese, *Physical Review B* **2010**, *81*, 045301.
- (29) Y. Kayanuma, *Physical Review B* **1988**, *38*, 9797-9805.

- (30) H. Mathieu, T. Richard, J. Allègre, P. Lefebvre, G. Arnaud, W. Granier, L. Boudes, J. L. Marc, A. Pradel, M. Ribes, *J. Appl. Phys.* **1995**, *77*, 287-293.
- (31) E. O. Kane, *J. Phys. Chem. Solids* **1957**, *1*, 249-261.
- (32) J. M. Luttinger, *Physical Review* **1956**, *102*, 1030-1041.
- (33) S. W. Koch, Y. Z. Hu, B. Fluegel, N. Peyghambarian, *J. Cryst. Growth* **1992**, *117*, 592-597.
- (34) S. Nomura, T. Kobayashi, *Physical Review B* **1992**, *45*, 1305-1316.
- (35) A. L. Efros, *Physical Review B* **1992**, *46*, 7448-7458.
- (36) A. I. Ekimov, F. Hache, M. C. Schanne-Klein, D. Ricard, C. Flytzanis, I. A. Kudryavtsev, T. V. Yazeva, A. V. Rodina, A. L. Efros, *J. Opt. Soc. Am. B* **1993**, *10*, 100-107.
- (37) A. Baldereschi, N. O. Lipari, *Physical Review B* **1973**, *8*, 2697-2709.
- (38) J.-B. Xia, *Physical Review B* **1989**, *40*, 8500-8507.
- (39) T. Richard, P. Lefebvre, H. Mathieu, J. Allègre, *Physical Review B* **1996**, *53*, 7287-7298.
- (40) Y. Kim, D.-J. Jang, *Chem. Commun.* **2013**, *49*, 8940-8942.
- (41) C. B. Murray, D. J. Norris, M. G. Bawendi, *J. Am. Chem. Soc.* **1993**, *115*, 8706-8715.
- (42) D. V. Talapin, A. L. Rogach, A. Kornowski, M. Haase, H. Weller, *Nano Lett.* **2001**, *1*, 207-211.
- (43) V. K. LaMer, R. H. Dinegar, *J. Am. Chem. Soc.* **1950**, *72*, 4847-4854.
- (44) D. V. Talapin, A. L. Rogach, M. Haase, H. Weller, *J. Phys. Chem. B* **2001**, *105*, 12278-12285.

- (45) M. Kahlweit, *Adv. Colloid Interface Sci.* **1975**, *5*, 1-35.
- (46) J. Park, J. Joo, S. G. Kwon, Y. Jang, T. Hyeon, *Angew. Chem. Int. Ed.* **2007**, *46*, 4630-4660.
- (47) T. Hyeon, S. S. Lee, J. Park, Y. Chung, H. B. Na, *J. Am. Chem. Soc.* **2001**, *123*, 12798-12801.
- (48) T. Hyeon, *Chem. Commun.* **2003**, 927-934.
- (49) S. G. Kwon, T. Hyeon, *Acc. Chem. Res.* **2008**, *41*, 1696-1709.
- (50) J.-Y. Kim, D. Lee, H. J. Kim, I. Lim, W. I. Lee, D.-J. Jang, *J. Mater. Chem. A* **2013**, *1*, 5982-5988.
- (51) J.-Y. Kim, S. J. Kim, D.-J. Jang, *J. Sep. Sci.* **2009**, *32*, 4161-4166.
- (52) N. Kuhnert, *Angew. Chem. Int. Ed.* **2002**, *41*, 1863-1866.
- (53) A. de la Hoz, A. Diaz-Ortiz, A. Moreno, *Chem. Soc. Rev.* **2005**, *34*, 164-178.
- (54) J.-S. Schanche, *Mol. Diversity* **2003**, *7*, 291-298.
- (55) K. Renggli, P. Baumann, K. Langowska, O. Onaca, N. Bruns, W. Meier, *Adv. Funct. Mater.* **2011**, *21*, 1241-1259.
- (56) J. Shin, R. M. Anisur, M. K. Ko, G. H. Im, J. H. Lee, I. S. Lee, *Angew. Chem. Int. Ed.* **2009**, *48*, 321-324.
- (57) N. Du, H. Zhang, J. Chen, J. Sun, B. Chen, D. Yang, *J. Phys. Chem. B* **2008**, *112*, 14836-14842.
- (58) M. Yan, F. Wang, C. Han, X. Ma, X. Xu, Q. An, L. Xu, C. Niu, Y. Zhao, X. Tian, P. Hu, H. Wu, L. Mai, *J. Am. Chem. Soc.* **2013**, *135*, 18176-18182.

- (59) M. Sanles-Sobrido, W. Exner, L. Rodríguez-Lorenzo, B. Rodríguez-González, M. A. Correa-Duarte, R. A. Álvarez-Puebla, L. M. Liz-Marzán, *J. Am. Chem. Soc.* **2009**, *131*, 2699-2705.
- (60) Y. Ma, L. Qi, J. Ma, H. Cheng, W. Shen, *Langmuir* **2003**, *19*, 9079-9085.
- (61) M. R. Kim, D.-J. Jang, *Chem. Commun.* **2008**, 5218-5220.
- (62) Z. Dai, J. Zhang, J. Bao, X. Huang, X. Mo, *J. Mater. Chem.* **2007**, *17*, 1087-1093.
- (63) Y. Yadong, R. M. Rioux, C. K. Erdonmez, S. Hughes, G. A. Somorjai, A. P. Alivisatos, *Science* **2004**, *5671*, 711-714.
- (64) W. Hou, S. B. Cronin, *Adv. Funct. Mater.* **2013**, *23*, 1612-1619.
- (65) M. A. Mahmoud, C. E. Tabor, M. A. El-Sayed, Y. Ding, Z. L. Wang, *J. Am. Chem. Soc.* **2008**, *130*, 4590-4591.
- (66) B. Lim, X. Lu, M. Jiang, P. H. C. Camargo, E. C. Cho, E. P. Lee, Y. Xia, *Nano Lett.* **2008**, *8*, 4043-4047.
- (67) M. A. Mahmoud, F. Saira, M. A. El-Sayed, *Nano Lett.* **2010**, *10*, 3764-3769.
- (68) J.-A. Kwak, D. K. Lee, D.-J. Jang, *Appl. Catal., B* **2013**, *142-143*, 323-328.
- (69) C. W. Yen, M. A. Mahmoud, M. A. El-Sayed, *J. Phys. Chem. A* **2009**, *113*, 4340-4345.

**Chapter 2. Direct Observation of Valence Band Splitting
Using Room Temperature Photoluminescence of CdS Hollow
Submicrospheres[†]**

[†] This is reproduced from Younshin Kim and Du-Jeon Jang, *Chem. Commun.* **2013**, 49, 8940-8942. © 2013 Royal Society of Chemistry.

2. 1. Abstract

The room-temperature photoluminescence spectra of CdS hollow submicrospheres prepared *via* employing silica hard templates and microwave irradiation present a profound insight on the quantum confinement-induced splitting of electron and hole states in the valence band. CdS hollow spheres with diameters within the submicrometer range with a very thin average shell thickness within the quantum confinement range have been studied. The nanocrystallite sizes calculated with data from HRXRD and absorption band edges fall within the strong confinement range, resulting in valence band splitting. The direct observation of this phenomenon at room temperature *via* photoluminescence has been interpreted by comparison to previous theoretical studies. The intensities of the observed 4 transitions match very well with literature values, but there has been a slight discrepancy regarding the magnitudes of the splittings. The lowest-energy bands have shown the highest sensitivity to nanoparticle size. The relative electron/hole state populations estimated by considering oscillator strengths of transitions have led to suggest that electron relaxation occurs faster than hole relaxation.

2.2. Introduction

With the exponential growth of interest in the field of nanochemistry, it has become increasingly important to characterize the optical and electronic properties of nanoparticles (NPs) as precisely as possible.¹⁻³ To the current day, many theoretical calculations based on the effective mass approximation (EMA) and the tight-binding theory have been carried out to predict the exact electronic structure of NPs.^{4,5} Recent computational investigations have been expanded to involve the Stokes shift of extremely small NPs, the role of strain for heterostructures, and the spin dynamics associated with valence-band mixing parameters.⁶⁻⁹ In support of this research, strenuous efforts have been taken in an attempt to observe the valence-band mixing phenomenon experimentally, yielding very unreliable minor results only.¹⁰⁻¹² In this chapter, the direct observation of the split degeneracy of hole states is reported and further interpreted to provide information on the electronic structure and relaxation of CdS hollow submicrospheres.

For II-VI semiconductor nanomaterials in general, the conduction band predominantly resembles the *s*-orbitals of the metal cation and that the valence band resembles the *p*-orbitals of the anion. As spin-orbit interactions are taken into consideration for the cubic nanostructures, the 6-fold degenerate valence band is split with the split-off energy of Δ_{SO} into two different bands: 4- and 2-fold degenerate bands corresponding to $J = 3/2$ and $1/2$, respectively. The degeneracies of these two bands will not be lifted unless NPs experience strong anisotropic effects and/or are within the strong confinement regime of ~ 2 exciton Bohr radii.¹³ When strong

confinement-induced valence-band mixing occurs, the degeneracy is further lifted and the hole wavefunctions become linear combinations of the different valence-band states with the mixed *s-d*-type symmetry.

CdS has recently shown much interest in displays, solar cells, and optoelectronic devices due to its unique photophysical and photochemical properties.¹⁴⁻¹⁶ CdS NPs not only have been experimentally studied largely, but also have been one of the most extensively computationally studied semiconductors, along with CdSe, for the investigation of the effects of valence-band mixing due to its relatively small band gap and small split-off energy.¹⁷⁻¹⁹ Due to distinct characteristics specified by tunable features such as shell thickness and interior cavity size, hollow structures are gaining current interest for potential applications as chemical reactors, drug-delivery carriers, energy-storage devices, and efficient catalysts.²⁰⁻²³ In this work, a facile silica hard-template method with the aid of microwave irradiation has been developed for the production of CdS hollow submicrostructures.

2.3. Experimental Section

2.3.1. Materials. Tetraethyl orthosilicate(1, >98%, TEOS) and ammonia(aq, 25%) were purchased from MERCK-Schuchardt; (3-aminopropyl)triethoxysilane(1, >98%, APTES), CdCl₂(s, tech grade) and Na₂S·9H₂O (s, >99.99%) were purchased from Sigma-Aldrich; 50% HF(aq) was purchased from J.T.Baker and diluted with water to

make 1% HF(aq); and glycerol(1, >99.0%) and ethanol(1, >99.0%) were purchased from Daejung Chemicals. Ultrapure deionized water (>17 MΩ cm) from a Millipore Milli-Q system was used throughout the experiments. Hard template silica submicrospheres were initially prepared by mixing 0.520 mL (2.35 mmol) TEOS and 0.313 mL (4.19 mmol, for H1) or 1.253 mL (16.7 mmol, for H2) ammonia(aq) in 8.33 mL ethanol and 3.00 mL water and stirring for 1.5 h; the relative sizes for the silica templates for H1 and H2 were controlled by adjusting the added amount of 25% ammonia(aq). To functionalize the surface of the silica submicrospheres, an excess amount of 1.94 mL (8.33 mmol) APTES was added to the sample and the mixture was further stirred for another 2 h. 159 mg (0.867 mmol) CdCl₂ was added as the cadmium source and stirred for 15 h at 60 °C. After centrifugation, half of the cadmium-attached silica spheres were redispersed in a mixture of 10.0 mL H₂O and 10.0 mL glycerol, and 104 g (0.433 mmol) Na₂S was added as the sulfur source. After stirring for 1 h, the mixture was put under microwave irradiation for 10 min with stirring every 20 s. After centrifugation, the resulting SiO₂@CdS core@shell structures were redispersed in 8.0 mL ethanol, submerged in 72 mL of 1% HF(aq) for 2 min, quickly diluted with water, and then centrifuged.

2.3.2. Characterization. Energy-filtered transmission electron microscopy (EFTEM) images were obtained with a Carl Zeiss LIBRA 120 microscope and the high-resolution transmission electron microscopy (HRTEM) image with a Tecnai F20 one. High-resolution x-ray diffraction (HRXRD) patterns were recorded using a Bruker D8 DISCOVER diffractometer with Cu K_α radiation ($\lambda = 0.154178$ nm). Extinction spectra were measured by using a Scinco S-3100 UV/vis spectrometer, and

photoluminescence (PL) spectra were obtained with a Princeton Instruments ICCD579G CCD detector attached to an Acton Research Spectrapro-500 spectrometer having a path length of 50 cm with excitation of 355 nm pulses having a duration time of 6 ns from a Quantel Brilliant Q-switched Nd:YAG laser.

2.4. Results and Discussion

By adjusting the sizes of silica hard templates, we have controlled the diameters of CdS hollow spheres easily. Two batches of different sizes were synthesized: one with an average outer diameter of 300 ± 25 nm and an average shell thickness of 11 ± 2 nm, and the other with an average outer diameter of 399 ± 8 nm and a typical shell thickness of 11 ± 1 nm (Figure 2-S1 in section 2.7). The former will now be referred to as H1 and the latter as H2 from this point on. In Figure 2-1, the EFTEM images of H1 and H2 show the overall clear-cut spherical hollow shape, and the HRTEM image of H2 clearly shows diffraction fringe patterns having quasispherical crystallite shapes of about 6.2 nm in average diameter with a lattice spacing of 0.336 nm that agrees very well with the standard spacing of 0.336 nm between the (111) lattice planes of the cubic zinc blende crystal lattice (JPCDS Card No. 04-008-8227). The cubic crystallinity of the CdS hollow submicrospheres is also confirmed by HRXRD data (Figure 2-S2 in section 2.7). The average crystallite sizes using the large HRXRD line

broadening at 2θ of 26.5° and the Scherrer equation²⁴ have been estimated to be 3.4 ± 0.1 nm for H1 and 3.6 ± 0.2 nm for H2.

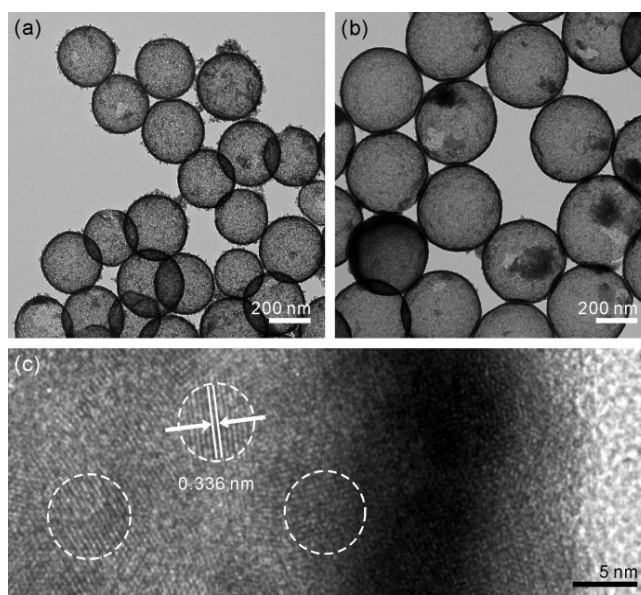


Figure 2-1. EFTEM images of CdS hollow microspheres H1 (a) and H2 (b) and HRTEM image of H2 (c), with the darkly shaded region representing the shell width. Each thin shell consists of CdS nanocrystallites as marked by dashed circles.

The modified Kubelka-Munk function states that $(\alpha hv)^2 = A(hv - E_g)^{25}$ where α is the absorption coefficient, A is a constant, and E_g is the band-gap energy. The extinction spectra of both samples were taken, and the subsequent $(\alpha hv)^2$ plots *vs.* hv have revealed the band-gap energies of 2.62 ± 0.04 eV for H1 and 2.58 ± 0.02 eV for H2 (Figure 2-2). The band-gap energies of the hollow microspheres are clearly larger than that of bulk CdS (2.42 eV), proving that the crystallites are indeed within the quantum confinement regime. Using the Brus equation^{26,27} for CdS NPs, we have

estimated the average diameters of the crystallites as 4.8 ± 1.0 nm for H1 and 5.2 ± 0.7 nm for H2. The differences in the size estimates from HRTEM, HRXRD, and extinction spectroscopy may arise from a number of factors; (1) only a very small number of crystallites has been employed in HRTEM, (2) the Scherrer equation assumes that all XRD broadening effects originate from size effects, (3) hidden hexagonal peaks in the HRXRD spectra may make the cubic peaks broader, and (4) the Brus equation doesn't account for the Stokes shift of extremely small NPs. Nevertheless, the radii of the CdS crystallites in both H1 and H2 would be less than twice the exciton Bohr radius of ~ 3 nm for CdS²⁷ in all cases, CdS crystallites in both samples are within the strong confinement regime, and valence-band mixing can be predicted for both samples.

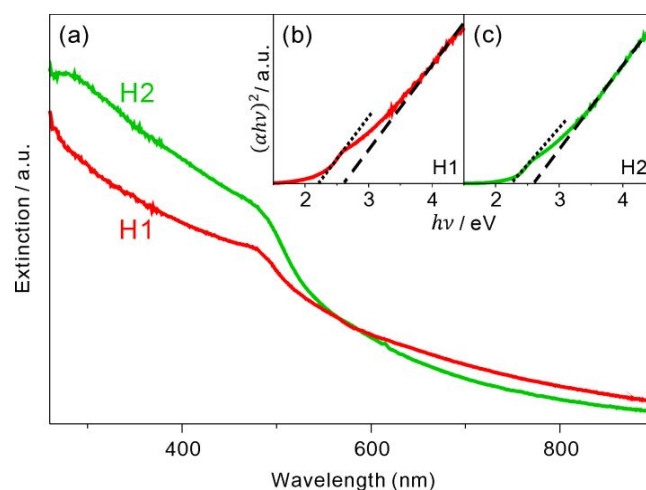


Figure 2-2. Extinction spectra of CdS hollow spheres H1 and H2 (a). $(\alpha hv)^2$ plots against hv after removal of scattering (c/λ^4 , where c is an arbitrary constant) from the extinction spectra to obtain the band gaps of H1 (b) and H2 (c). The intercept of a dashed line corresponds to the actual CdS band gap while that of a dotted line corresponds to the energy gap created by sulfur-vacancy defects.

The dotted intercepts in the $(ah\nu)^2$ plots *vs.* $h\nu$ of Figure 2-2 can be assigned to energy gaps between the valence bands and possible surface states created by sulfur-vacancy defects. The surface-state band-gap energies of 2.20 ± 0.03 eV for H1 and 2.26 ± 0.02 eV for H2 obtained from the extinction spectra agree very well with the well-known sulfur-vacancy energy gap of 2.2 eV.²⁸ This transition is also visible as a weak broad shoulder band that has not been fitted in the PL spectra of CdS hollow microspheres (see below).

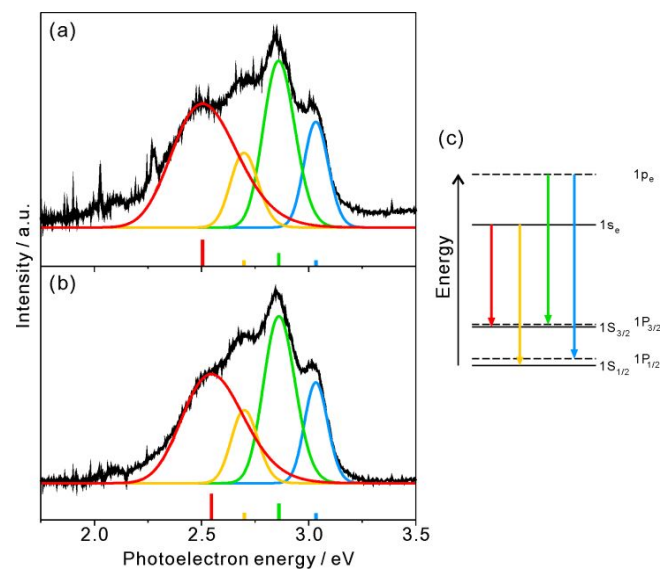


Figure 2-3. PL spectra of H1 (a) and H2 (b) suspended in ethanol with excitation at 355 nm. The solid lines correspond to the deconvoluted Gaussian curves and the integrals of Gaussian-fitted curves are shown relatively as vertical lines at the bottom. The exact locations and integrals of the fitted curves are outlined in Table 2-1, and the associated transitions are described in a band-energy diagram (c).

Each PL spectrum, with excitation at 3.493 eV, of both H1 and H2 has been fitted into four distinct Gaussian curves, which have been assigned to four theoretically reported²⁹ transitions: $1s_e \rightarrow 1S_{3/2}$, $1s_e \rightarrow 1S_{1/2}$, $1p_e \rightarrow 1P_{3/2}$, and $1p_e \rightarrow 1P_{1/2}$ (Figure 2-3; Table 2-1). Because the maxima of three of the four curves lie above the band-gap energy calculated from the extinction spectrum, it can be understood that the peaks do not originate from defect sites or surface states. Three of the four transitions for H1 energetically correspond very well within 2 meV to the respective ones for H2, but the transition energy of $1s_e \rightarrow 1S_{3/2}$ in H1 is lower by 41 meV than that in H2. This suggests that the energy of the $1S_{3/2}$ hole state in the valence band is affected most significantly by size changes.

Table 2-1. Peak positions and integrated intensity values of the fitted Gaussian curves in Figure 2-3.

Transitions	H1		H2	
	Position (eV)	Intensity (a.u.)	Position (eV)	Intensity (a.u.)
$1s_e \rightarrow 1S_{3/2}$	2.505 ± 0.151^a	1.00	2.546 ± 0.143^a	1.00
$1s_e \rightarrow 1S_{1/2}$	2.698 ± 0.064	0.22	2.700 ± 0.062	0.26
$1p_e \rightarrow 1P_{3/2}$	2.860 ± 0.073	0.50	2.861 ± 0.073	0.62
$1p_e \rightarrow 1P_{1/2}$	3.034 ± 0.056	0.22	3.034 ± 0.054	0.24

^aThe Stokes shift of H1 is 115 meV while that of H2 is 34 meV. The large difference in magnitudes of the Stokes shift between two samples arises from differences in nanocrystallite sizes and nanocrystallite size distributions.

In interpretation of the PL spectra, it is assumed that the inhomogeneous Gaussian broadening caused by the size distribution is the dominant source of broadening in comparison to very small Lorentzian broadening created by light

polarization due to the random orientation of NPs in space.⁵ Because the band gap of semiconductor NPs is extremely sensitive to size, most quantum dots (QDs) in the literature exhibit broad emission bands with an average half width at the half maximum (HWHM) of greater than 200 meV, corresponding to a standard deviation of 170 meV.¹⁴⁻¹⁶ In our spectra, it is noticeable that only the $1s_e \rightarrow 1S_{3/2}$ transition exhibits HWHM of 180 (H1) and 170 meV (H2) that agree well with the average broadening of QDs although HWHM of the three others (~ 80 meV) are significantly smaller. The fact that a line width reflects the spread of an energy level suggests that the hole state of $1S_{3/2}$ involved in the $1s_e \rightarrow 1S_{3/2}$ transition is energetically affected most sensitively by the size distribution. The greater sensitivity of the $1S_{3/2}$ hole state to size is believed to be correlated to the general idea that energetically lower hole states are more sensitive to size.

The relative integrals of the fitted curves also confirm the respective assignment of the transitions, as the intensity of a transition contains information on the populations of the initial and the final states as well as on the oscillator strength of the transition. The integrated intensities of the $1s_e \rightarrow 1S_{3/2}$ and $1p_e \rightarrow 1P_{3/2}$ peaks are respectively about 4 and 2 times larger than those of the $1s_e \rightarrow 1S_{1/2}$ and $1p_e \rightarrow 1P_{1/2}$ peaks. This indicates that the number of holes in $1L_{3/2}$, where L is S or P, recombining with electrons in the conduction band is much larger than that in $1L_{1/2}$. When the relative intensities of two absorption transitions with a common upper state are known, the relative intensities of their two corresponding PL transitions may be used to estimate the relative hole population of $1L_{1/2}$ to $1L_{3/2}$. Likewise, the relative intensities of PL transitions with a common lower state can depict the relative electron population

of $1p_e$ to $1s_e$, assuming that hole states with the same J quantum number will have roughly the same population. By normalizing the intensity ratio of two transitions with a common state in our PL spectra to the theoretically predicted ratio of the two corresponding transitions in absorption spectra,²⁹ the relative electron population of $1p_e$ to $1s_e$ (N_{p_e}/N_{s_e}) and the relative hole population of $1L_{1/2}$ to $1L_{3/2}$ ($N_{1/2}/N_{3/2}$) have been calculated and summarized in Table 2-2. Despite calculating N_{p_e}/N_{s_e} separately using transitions to different J values, N_{p_e}/N_{s_e} can be approximated to a constant value of 0.5. Similarly, using transitions from different electron states, $N_{1/2}/N_{3/2}$ was also approximated to 0.7. Both values are consistently less than 1, confirming that higher energy states have a lower population in comparison to lower energy states. Also, the fact that $N_{1/2}/N_{3/2}$ is greater than N_{p_e}/N_{s_e} presents the idea that electron relaxation in CdS hollow microspheres dispersed in ethanol occurs relatively faster than hole relaxation. It is noteworthy that although PL at the band edge of CdS NPs decays within several picoseconds,³⁰ hole lifetimes have been reported to increase up to several nanoseconds in closely spaced QD structures.³¹

Although the calculated intensities of ref. 29 show the practical proof of the good assignment of our PL peaks, it should be realized that there is quite a large discrepancy regarding the magnitude of splitting as compared to the literature. Díaz *et al.* claim that the largest calculated energy gap between the $1S_{3/2}$ and $1S_{1/2}$ hole states is 132 meV,²⁹ whereas our experimental results show a splitting of 193 (H1) and 154 meV (H2). Several other resources also predict smaller splitting, but it is a widely accepted fact that the band splitting is very sensitive to EMA Luttinger parameters, which for CdS

are still ambiguous.²⁹ The parameters may fail to incorporate the effects of the particular structure of CdS hollow microspheres and the effects of the close contact of the nanocrystallites comprising the hollow spheres. In fact, the experimental data obtained by Samokhvalov *et al.* show a splitting of ~ 200 meV, more similar to our results.¹¹ It is believed that the particular structure of our CdS hollow spheres allows for these transitions to be seen. As the silica core is etched out, it is expected that some of the silica particles remain to protect CdS NPs from aggregating and also to obstruct the relaxation pathways of excited electrons and holes.

Table 2-2. Relative electron population of $1p_e$ to $1s_e$ (N_{p_e}/N_{s_e})^a and relative hole population of $1L_{1/2}$ to $1L_{3/2}$ ($N_{1/2}/N_{3/2}$).^b

Sample	N_{p_e}/N_{s_e}		$N_{1/2}/N_{3/2}$	
	$1L_{3/2}^c$	$1L_{1/2}^c$	$1s_e^d$	$1p_e^d$
H1	0.48	0.49	0.69	0.71
H2	0.60	0.48	0.81	0.65

^a Calculated by normalizing the relative transition strength of $1p_e$ and $1s_e$ to a common lower state with the theoretical¹⁵ relative absorption strength of the common lower state to the corresponding upper states.
^b Calculated by normalizing the relative transition strength of $1L_{1/2}$ and $1L_{3/2}$ from a common upper state with the theoretical¹⁵ relative absorption strength of the corresponding lower states to the common upper state, where L is S or P. ^c Common lower state. ^d Common upper state.

2.5. Conclusion

CdS hollow spheres of submicrometer size with a very thin average shell thickness of 11 nm was successfully synthesized *via* employing silica hard templates

and microwave irradiation. Despite the large overall size, the hollow structures showed ‘nano’ characteristics distinctively. Confinement-induced valence-band mixing was directly observed through PL spectra for the first time without using complex spectroscopic techniques at non-delicate conditions.

2.6. Acknowledgements

This work was supported by research grants by the National Research Foundation (NRF) of Korea (2012-006345 and 2011-0028981). D.J.J. is also thankful to the SRC program of NRF (2007-0056331).

2.7. Supporting Information

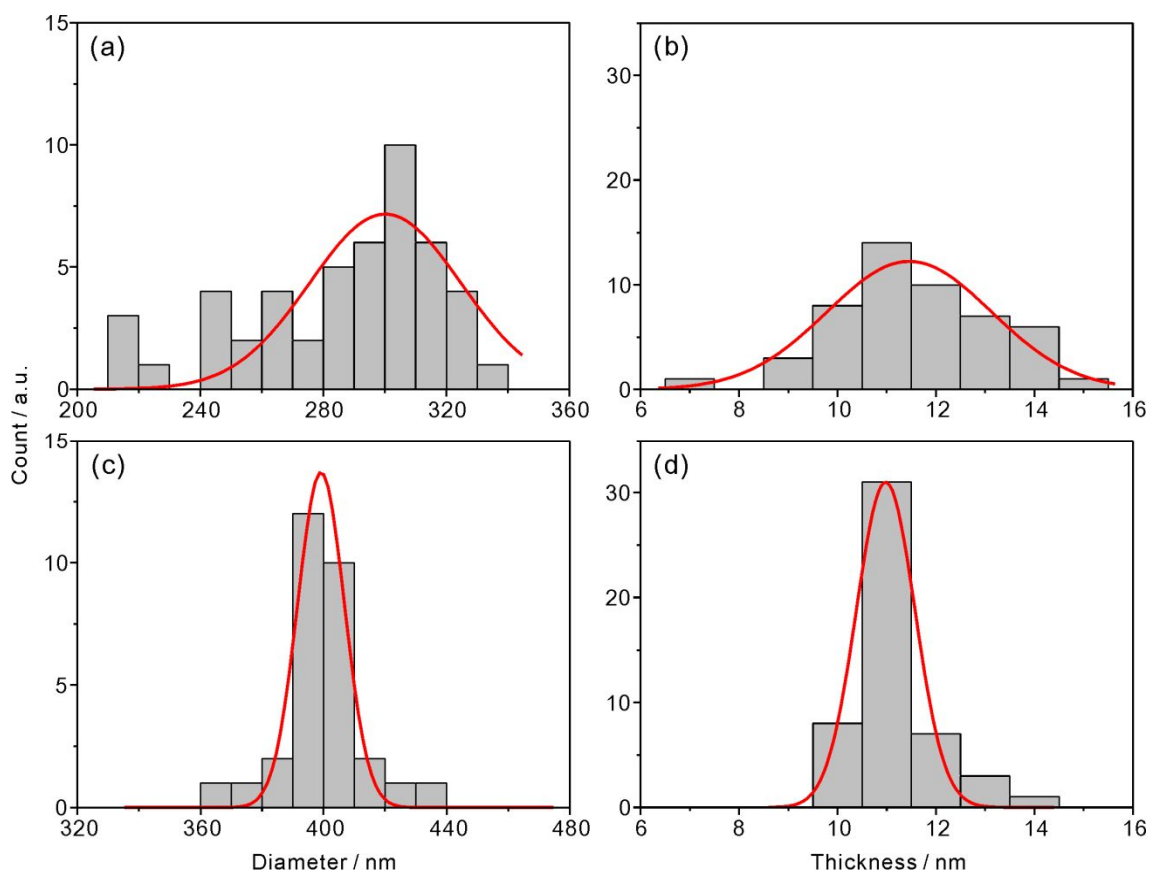


Figure 2-S1. Histograms showing to the outer diameters (left) and the shell thicknesses (right) of CdS hollow microspheres H1 (top) and H2 (bottom). H1 showed an average diameter of 300 ± 25 nm (a) and an average shell thickness of 11 ± 2 nm (b) while H2 showed an average diameter of 399 ± 8 nm (c) and an average shell thickness of 11 ± 1 nm (d).

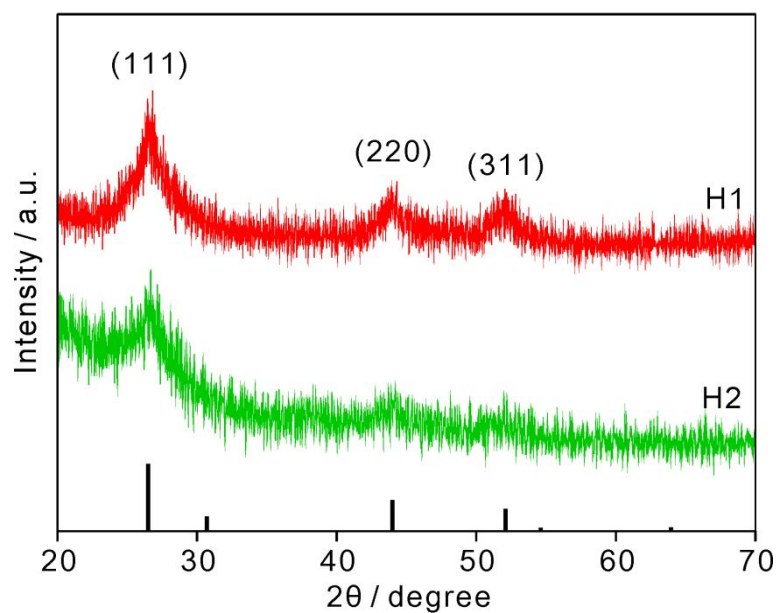


Figure 2-S2. HRXRD spectra of H1 (red) and H2 (green) revealing the cubic zinc blende crystal lattice (reference shown at the bottom, JPCDS Card No. 04-008-8227).

2.8. References

- (1) S.-Y. Park, H. Jeong, H. Kim, J. Y. Lee, D.-J. Jang, *J. Phys. Chem. C*, **2011**, *115*, 24763.
- (2) Y. Kim, J.-Y. Kim, D.-J. Jang, *J. Phys. Chem. C*, **2012**, *116*, 10296.
- (3) H.-B. Kim, D.-J. Jang, *CrystEngChem*, **2012**, *14*, 6946.
- (4) M. Nirmal, D. J. Norris, M. Kuno, M. G. Bawendi, A. L. Efros, M. Rosen, *Phys. Rev. Lett.*, **1995**, *75*, 3728.
- (5) T. Richard, P. Lefebvre, H. Mathieu, J. Allegre, *Phys. Rev. B*, **1996**, *53*, 7287.
- (6) D. O. Demchenko, L.-W. Wang, *Phys. Rev. B*, **2006**, *73*, 155326.
- (7) J. G. Diaz, M. Zieliński, W. Jaskólski, G. W. Bryant, *Phys. Rev. B*, **2006**, *74*, 205309.
- (8) P. Horodyská, P. Němec, D. Sprinzl, P. Malý, V. N. Gladilin, J. T. Devreese, *Phys. Rev. B*, **2010**, *81*, 45301.
- (9) H. Tong, M. W. Wu, *Phys. Rev. B*, **2011**, *83*, 235323.
- (10) K. I. Kang, B. P. McGinnis, Sandalphon, Y. Z. Hu, S. W. Koch, N. Peyghambarian, A. Mysyrowicz, L. C. Liu, S. H. Risbud, *Phys. Rev. B*, **1992**, *45*, 3465.
- (11) A. Samokhvalov, M. Berfeld, M. Lahav, R. Naaman, E. Rabani, *J. Phys. Chem. B*, **2000**, *104*, 8631.
- (12) A. P. J. Stampfl, Ph. Hofmann, O. Schaff, A. M. Bradshaw, *Phys. Rev. B*, **1997**, *55*, 9679.
- (13) Y. Kayanuma, *Phys. Rev. B*, **1988**, *38*, 9797.

- (14) X. Xu, Y. Zhao, E. J. Sie, Y. Lu, B. Liu, S. A. Ekahana, X. Ju, Q. Jiang, J. Wang, H. Sun, T. C. Sum, C. H. A. Huan, Y. P. Feng, Q. Xiong, *ACS Nano*, **2011**, *5*, 3660.
- (15) R. F. Oulton, V. J. Sorger, T. Zentgraf, R.-M. Ma, C. Gladden, L. Dai, G. Bartal, X. Zhang, *Nature*, **2009**, *461*, 629.
- (16) Q. Shen, Y. Liu, J. Xu, C. Meng, X. Liu, *Chem. Commun.*, **2010**, *46*, 5701.
- (17) S. W. Koch, Y. Z. Hu, B. Fluegel, N. Peyghambarian, *J. Cryst. Growth*, **1992**, *117*, 592.
- (18) J. Li, J.-B. Xia, *Phys. Rev. B*, **2000**, *62*, 12613.
- (19) B. Yang, J. E. Schneeloch, Z. Pan, M. Furis, M. Achermann, *Phys. Rev. B*, **2010**, *81*, 73401.
- (20) S. J. Kim, C. S. Ah, D.-J. Jang, *Adv. Mater.*, **2007**, *19*, 1064.
- (21) M. R. Kim, D.-J. Jang, *Chem. Commun.*, **2008**, 5218.
- (22) M. R. Kim, J.-Y. Kim, S. J. Kim, D.-J. Jang, *Appl. Catal. A: Gen.*, **2011**, *393*, 317.
- (23) M. R. Kim, D. K. Lee, D.-J. Jang, *Appl. Catal. B: Environ.*, **2011**, *103*, 253.
- (24) J. I. Langford, A. J. C. Wilson, *J. Appl. Cryst.*, **1978**, *11*, 102.
- (25) L. Li, Y.-W. Yang, G.-H. Li, L.-D. Zhang, *Small*, **2006**, *2*, 548.
- (26) H. Y. Acar, R. Kas, E. Yurtsever, C. Ozen, I. Lieberwirth, *J. Phys. Chem. C*, **2009**, *113*, 10005.
- (27) L. E. Brus, *J. Chem. Phys.*, **1984**, *80*, 4403.
- (28) Q. Xiao, C. Xiao, *Appl. Surf. Sci.*, **2009**, *255*, 7111.

- (29) J. G. Díaz, J. Planelles, G. W. Bryant, J. Aizpurua, *J. Phys. Chem. B*, **2004**, *108*, 17800.
- (30) M. D. Garrett, A. D. Dukes III, J. R. McBride, N. J. Smith, S. J. Pennycook, S. J. Rosenthal, *J. Phys. Chem. C*, **2008**, *112*, 12736.
- (31) K. Gawarecki, P. Machnikowski, *Phys. Rev. B*, **2012**, *85*, 41305.

Chapter 3. Facile Microwave Fabrication of CdS Nanobubbles with Highly Efficient Photocatalytic Performances

3. 1. Abstract

A new fabrication method of CdS nanobubbles with high photocatalytic activity has been explored under ambient conditions using SiO₂ hard templates and microwave irradiation. The one-step Stöber method has been used to produce SiO₂ core nanospheres, onto which CdS shells have been readily and efficiently coated by 10 min microwave irradiation. The acid etching of the SiO₂ cores has produced monodisperse CdS nanobubbles with outer diameters of 300, 370, and 400 nm with a uniform shell thickness of 11 nm. The CdS nanobubbles have been found to photocatalyze the degradation of rhodamine B efficiently under Xe-lamp irradiation *via* simultaneous reaction pathways of N-deethylation and conjugated-ring attack. It has been found that the degradation rate increases linearly with the concentration increase of the nanocatalyst but decreases nonlinearly with increasing nanobubble diameters. The pseudo-first-order degradation rate constant *via* the nanobubbles (0.081 min⁻¹) was found to be about 20 times larger than that *via* the SiO₂@CdS core@shell nanocomposites (0.0044 min⁻¹) due to nanoreactor confinement effect leading to decrease in the activation energy of the reaction.

3.2. Introduction

With the continuous depletion of conventional energy resources, conversion of light energy into chemical, mechanical, and electrical energy has become a rising interest in the movement for environmental sustainability and green chemistry.¹ In particular, nanomaterials have become increasingly popular for use as photocatalysts in a variety of applications such as water splitting,²⁻³ CO₂ reduction,⁴ and syntheses.⁵ Among the diversity of applications, the photocatalytic degradation of organic contaminants is a powerful solution to wastewater treatment due to a lack of waste-disposal problems, low cost, and the simplicity of the whole system.⁶ The decomposition of organic dyes is also used to model the photocatalytic activity of photocatalysts in general.⁷⁻¹⁰

In semiconductor-mediated degradation of non-biodegradable organic materials, photocatalysis usually occurs through two different pathways: (1) direct semiconductor photocatalysis where the semiconductor is photoexcited and (2) indirect semiconductor photocatalysis where the substrate or dye is photoexcited.¹¹⁻¹³ For the pathway 1, an electron is promoted from the valence band to the conduction band when the radiation energy supplied onto the semiconductor is higher than the band gap, resulting in an electron-hole pair. When this photoexcited state of the semiconductor is prolonged long enough, the excited electron and hole are able to migrate to the surface of the semiconductor to facilitate redox reactions, forming very strong oxidants: the superoxide radical (O₂^{·-}), the hydroperoxyl radical (HO₂[·]), and the hydroxyl radical (OH[·]).¹⁴ For the pathway 2, light absorption facilitates the excitation

of the dye or substrate into an excited state with a reduction potential negative enough for electron injection into the conduction band of the semiconductor. Often, this separation of charges allows for the electron to proceed to reduce oxygen molecules into reactive superoxide radicals. All of the aforementioned reactive oxygen species are able to degrade a variety of pollutants readily into environmentally benign and simple molecules.

Although TiO_2 is generally the popular choice of materials for photocatalysis, it has an indirect large band gap of 3.0~3.2¹⁵ eV within the ultraviolet (UV) range, which tolerates a maximum of only 4% of solar radiation energy. On the other hand, CdS has a direct band gap of 2.42 eV¹⁶ that allows for the high absorption of both UV and visible light, which contributes to about 43% of solar radiation energy.¹⁷ Due to these advantages, CdS has been gaining popularity as a photocatalyst for a variety of reactions. Zhang et al. have recently synthesized CdS sheets for the selective activation of saturated sp^3 C-H bonds under ambient conditions,¹⁸ Chen et al. have reported the self-assembly of CdS-nanospheres/graphene hybrid nanocomposites for selective nitro-organic reduction,⁵ and Li et al. have synthesized CdS clusters-decorated graphene sheets for efficient H_2 production.¹⁷

The shape of a nanophotocatalyst also plays a big role on its photocatalytic performance. It has been reported that solid metallic catalysts with sharp tips or hollow structures reveal a large enhancement in their catalytic activity.¹⁹ In particular, extended studies¹⁹⁻²¹ have shown that besides the enhancement due to an increased surface-to-volume ratio, additional enhancement effects occur for hollow structures. The nanoreactor confinement effect, otherwise known as the nanocage effect, occurs

due to two main factors: increase in the concentration of the reaction intermediate within the cavity of the hollow nanocatalyst and possibility of catalytically more-active sites within the inner surface of the hollow nanocatalyst.¹⁹ A variety of researches on hollow nanostructures have been reported recently: photocatalytic CdSnO₃·3H₂O hollow-nanocuboids have been synthesized by a template-free microwave hydrothermal method for the mineralization of gaseous benzene,⁸ mesoporous TiO₂ hollow shells have been used to degrade organic dyes,²² and platinum nanobubbles have been shown to enhance catalytic degradation performances due to the nanoreactor confinement effect.²³

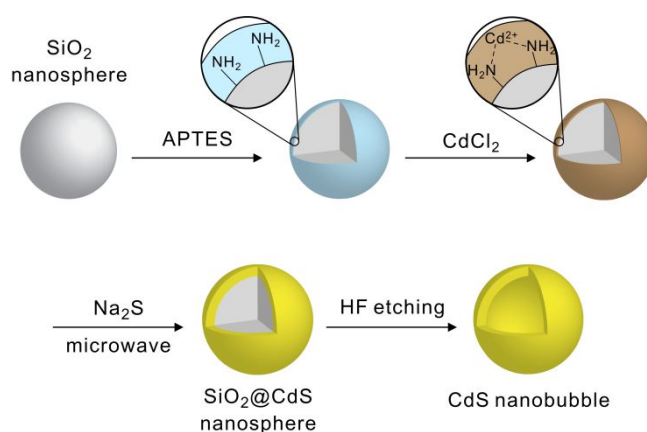


Figure 3-1. Schematic for the synthesis of a CdS nanobubble *via* a hard-template method with the assistance of microwave irradiation.

In this present work, a new fabrication method of CdS hollow structures *via* microwave irradiation has been explored, resulting in well-defined discrete nanobubble structures with diameters ranging in the submicrometer scale but with a

shell thickness within the quantum confinement range (Figure 3-1). The straightforward conventional hard-template method used in our experiments involves five major steps: (1) preparation of SiO₂ hard templates, (2) their surface functionalization, (3) coating of the templates with designated precursors, (4) microwave treatment for CdS crystallization, and (5) selective removal of the initial hard templates. Microwave irradiation allows for the quick homogeneous formation of a thin crystalline CdS shell around a SiO₂ template core within just 10 minutes while as the hydrothermal method would require hours in an autoclave.²⁴ Because silica nanospheres with well-known synthetic processes have a narrow size distribution and good availability, they have been used as templates to fabricate three different batches of CdS nanobubbles with varying diameters. These CdS nanobubbles have been found to photocatalyze the degradation of rhodamine B (RhB) with remarkable efficiency in comparison to SiO₂@CdS core@shell nanocomposites and other reported CdS photocatalysts due to nanoreactor confinement effects.

3.3. Experimental Section

3.3.1. Materials. Chemicals were used as received: tetraethyl orthosilicate (TEOS, 1, >98%), (3-aminopropyl)triethoxysilane (APTES, 1, >98%), CdCl₂(s, tech grade), and Na₂S·9H₂O(s, >99.99%) from Sigma-Aldrich; ammonia(aq, 25%) from MERCK-Schuchardt; RhB(s) from Wako Pure Chemical; 50% HF(aq) from J.T.Baker;

and glycerol(1, >99.0%) and ethanol(1, >99.0%) from Daejung Chemicals. Ultrapure deionized water (>17 M Ω cm) from a Millipore Milli-Q system was used throughout the experiments.

3.3.2. Preparation of CdS Nanobubbles. All synthetic processes of CdS nanobubbles were carried out under ambient conditions. Hard-templates of silica nanospheres were initially prepared following the Stöber method,²⁵ in which the relative sizes of the silica templates were controlled by adjusting the added amount of 25% ammonia(aq). A mixture of TEOS (0.26 mL), 25% ammonia(aq) (0.16 mL for B300, 0.31 mL for B370, and 0.63 mL for B400), ethanol (4.17 mL), and water (1.50 mL) was stirred for 1.5 h. To functionalize the surface of the silica nanospheres with amino groups, an excess amount of APTES (0.98 mL) was added to the sample and the mixture was further stirred for another 2 h. CdCl₂ (80 mg) was added as the cadmium source and stirred for 15 h at 60 °C for the coordination of Cd²⁺ cations onto the amino-functionalized silica nanosphere surface. After centrifugation at 10,000 rpm for 10 min, the cadmium-attached silica nanospheres were redispersed in a mixture of H₂O (10.0 mL), glycerol (10.0 mL), and Na₂S (104 mg). After being stirred for 1 h, the mixture contained in a 50 mL vial was subject to irradiation by a Samsung HV-367AWJ microwave system (2.45 GHz, 300 W) for 10 min, by repeating sets of irradiation (20 s) followed by stirring outside the microwave system (15 s) for 30 times. The solution was cooled (~5 min) before repeatedly centrifuging and washing with a 1:1 mixture of water and ethanol for three times. The resulting SiO₂@CdS core@shell structures were resuspended in ethanol (8.0 mL). A 2 mL portion of this dispersion

was submerged in 18 mL of 1% HF(aq) for 2 min, and it was repeatedly centrifuged and washed with water and ethanol for 3 times.

3.3.3. Characterization. Low-resolution transmission electron microscopic (TEM) images were obtained by an energy-filtered microscope (Carl Zeiss, LIBRA 120) while high-resolution TEM (HRTEM) images, fast Fourier transform (FFT) patterns, and energy-dispersive X-ray (EDX) elemental profiles and mappings were obtained by a high-resolution microscope (FEI, Tecnai F20) equipped with an EDX spectroscope. High-resolution X-ray diffraction (HRXRD) patterns were recorded using a diffractometer (Bruker, D8 DISCOVER, Cu K_{α} radiation, $\lambda = 0.154178$ nm) in a 2θ range from 20° to 70° . X-ray photoelectron spectroscopic (XPS) data were obtained using with a photoelectron spectrometer (KRATOS, AXIS-HSi) with a 150 W Mg anode with a scan step of 0.1 eV. Extinction spectra were measured by using a UV/vis spectrometer (Scinco, S-3100), and photoluminescence (PL) spectra were obtained with a CCD (Princeton Instruments, ICCD579G) attached to a 0.5 m spectrometer (Acton Research, Spectrapro-500) with excitation of 355 nm pulses having a duration time of 6 ns from a Q-switched Nd:YAG laser (Quantel, Brilliant).

3.3.4. Photocatalytic Experiments. All the experiments were carried out in 10 mm x 10 mm plastic cuvettes (Kartell, PMMA UV grade) under ambient conditions. An aqueous suspension of 1.5 mL containing a nanocatalyst (0.10 g L^{-1}) and RhB ($1 \times 10^{-5} \text{ M}$) was magnetically stirred in the dark for 1 h to ensure the adsorption-desorption equilibrium of RhB on the nanocatalyst surface. The mixture was placed 20 cm away from a 300 W Xe arc lamp (Schoeffel, LPS 255 HR), with the light beam to cover the entire face of the solution directly facing the light source, and magnetically

stirred during irradiation for a specific period; the light irradiance was fixed at 63 mW cm⁻². The irradiated reaction mixture was centrifuged (10000 rpm, 10 min) to separate the supernatant, whose UV/vis absorption spectrum was then measured to monitor the concentration of remnant RhB.

3.4. Results and Discussion

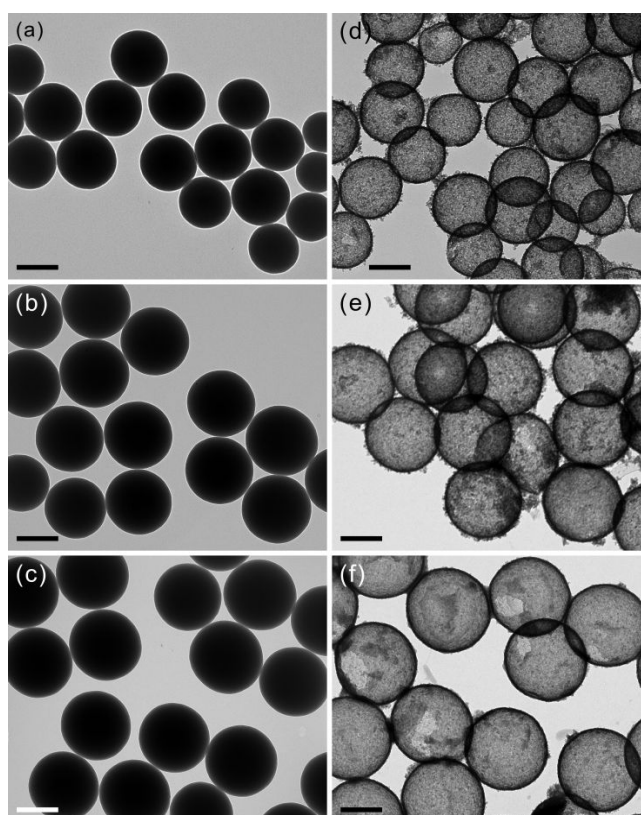


Figure 3-2. TEM images for the silica nanosphere templates of T300 (a), T370 (b), and T400 (c) and the corresponding CdS nanobubbles of B300 (d), B370 (e), and B400 (f). Each scale bar indicates 200 nm.

3.4.1. Microscopic Characterization. By controlling the amount of the base catalyst of the Stöber method,²⁵ the diameters of the hard-template silica nanosphere have been well-controlled. As shown in Figure 3-2, spherical silica hard templates of T300, T370, and T400 having average diameters of 270 ± 20 , 330 ± 10 , and 350 ± 10 nm, respectively, have been used to fabricate the corresponding CdS nanobubbles of B300, B370, and B400 having average outer diameters of 300 ± 20 , 370 ± 10 , and 400 ± 10 nm, respectively; the shells of all the CdS nanobubbles have a uniform thickness (t) of 11 ± 2 nm. The inner radii of the CdS nanobubbles are about 6% larger than the radii of the corresponding templates on average due to the surface treatment of the templates with APTES (Figure 3-1). The contrast between the brighter inner cores and the well-defined dark circular outlines clearly indicates that the CdS nanobubbles are structurally hollow indeed. Comparison of the TEM images of the nanobubbles with the respective ones of SiO₂@CdS core@shell nanocomposite structures of C300, C370, and C400 (Figure 3-S1 in section 3.7), from which B300, B370, and B400, respectively, have been produced, also indicates that the core templates have been completely etched out in the nanobubbles. Although it is difficult to distinguish the core@shell structure, the darker outline of the denser CdS shell can be noticed with careful examination.

The HRTEM image of Figure 3-3a shows better-defined shapes of B370 CdS nanobubbles. The shells are not entirely smooth in nature, but comprise of small CdS nanoparticles aggregated together to form the nanobubbles. However, the smooth shaded parts between the nanobubbles are due to remnant silica nanoparticles that have been etched out by HF but aggregated again (see below). As CdS is known for its

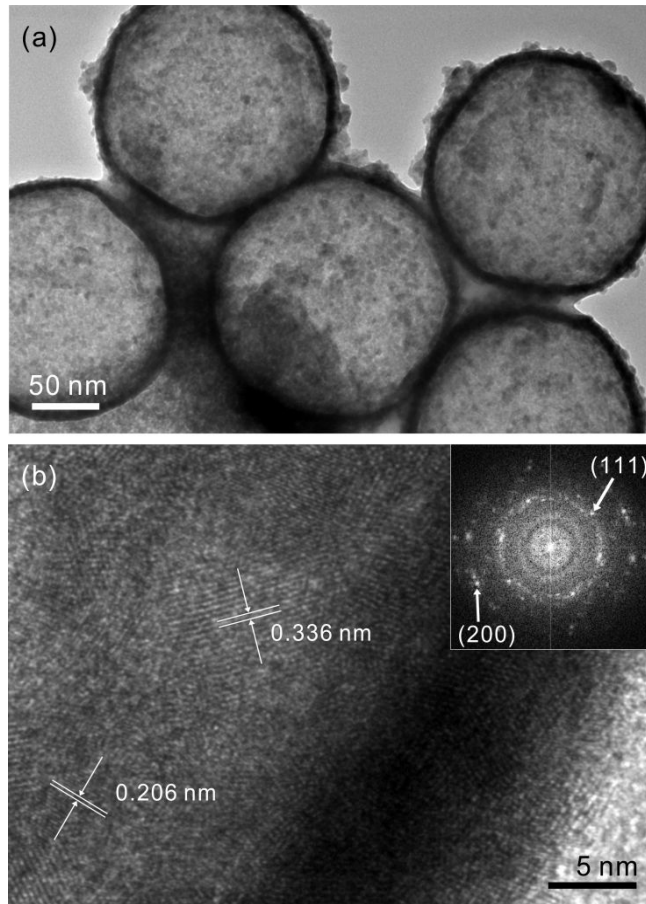


Figure 3-3. HRTEM images of CdS nanobubbles B370 at lower (a) and higher (b) magnification. The inset in b shows the FFT pattern of the selected area.

instability in water,⁶ these remaining silica nanoclusters may actually play a role in the stability of the CdS nanobubbles, protecting them from aggregation. Figure 3-3b shows a HRTEM image with higher magnification, depicting the high crystallinity of a CdS nanobubble. The diffraction fringe patterns show d-spacings of 0.336 nm and 0.206 nm that correspond precisely to the standard spacings of 0.336 nm and 0.206 nm between the (111) and (220) lattice planes, respectively, of the cubic zinc blende crystal lattice of CdS (JPCDS Card No. 04-008-8227). The d-spacings of 0.336 nm

and 0.291 nm measured from the FFT pattern in the inset of Figure 3-3b correspond to the standard spacing between the (111) and (200) lattice planes, respectively, of the reference cubic CdS. The ring-like FFT pattern portrays polycrystallinity in the nanobubble. The magnified HRTEM images and the FFT patterns of B300 and B400 (Figure 3-S2 in section 3.7) also show that CdS nanobubbles have the cubic zinc blende crystal structure.

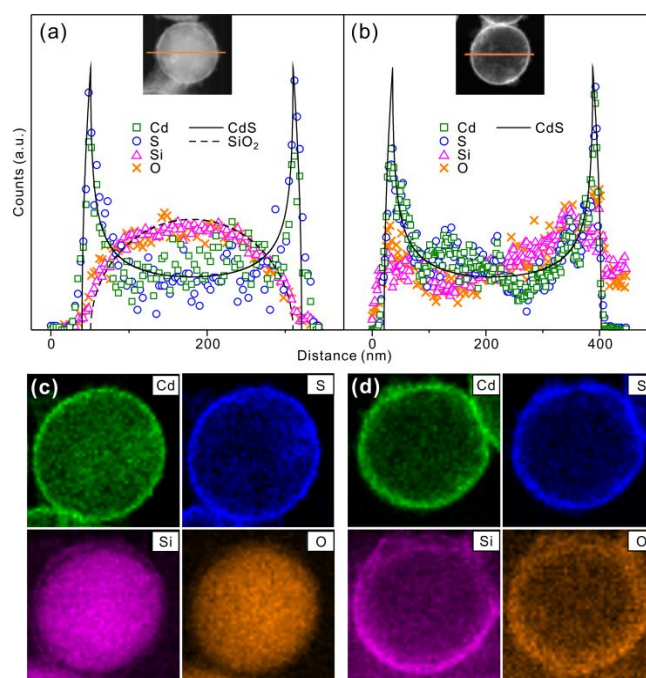


Figure 3-4. Area-normalized EDX elemental profiles of C300 (a) and B370 (b) scanned along the lines in the HAADF images of the insets; symbols indicate experimental data while lines represent theoretical fittings. Elemental mapping profiles of Cd, S, Si, and O for C300 (c) and B370 (d).

The EDX line-scanned elemental profiles of C300 and B370 have been examined to verify the exact structures and compositions of a $\text{SiO}_2@\text{CdS}$ nanocomposite and a CdS nanobubble, respectively (Figure 3-4a,b). The intensity profiles of Cd and S for both C300 and B370 exhibit two characteristic sharp peaks representing the dense edges of nanoshells. The shapes of the intensity profiles for Si and O in the nanocomposite are drastically different from the respective ones in the nanobubble. The line-scanned elemental intensity profiles have been theoretically fitted by equations derived simply from core@shell and hollow spheres. The shape of Si and O for C300 was fitted to a circle with $d = 259$ nm, suggesting that the silica core exists in a spherical shape. The fitting of Cd and S for C300 has represented a CdS shell with a shell thickness of 11 nm and an outer diameter of 281 nm. Similarly, the intensity profiles of Cd and S for B370 were fitted to a theoretical CdS nanobubble with a shell thickness of 15 nm and an outer diameter of 382 nm. However, the shapes of the Si and O intensity profiles for B370 no longer match with the shape of a core or shell, revealing that the SiO_2 particles of B370 exist in an irregular shape around the CdS shell. The silica intensity profile shows a pronounced decrease at positions where the two peaks of CdS exist, revealing that CdS and SiO_2 are present as separate entities and that remnant silica particles are surrounding the CdS shell. The atomic ratios of Cd to S estimated from the EDX profiles is 1.4 for C300 and 1.3 for B370. Deviations from the theoretical ratio of 1 for CdS may arise from the binding of Cd with O atoms and/or sulfur vacancy defects in the CdS shell. It is also deduced that the etching process helps to purify CdS nanoshells.

The Cd, S, Si, and O elemental mapping profiles of Figure 3-4c,d have also been compared to understand the structures of C300 and B370. The Cd and S elemental maps for both C300 and B370 show a defined line in the shape of a circle with lower intensities inside the circle, representing a hollow nanoshell. However, the elemental maps of Si and O are distinctly different for the two samples; the elemental maps for C300 show brightly filled circles with radii smaller than those of the Cd and S elemental maps while the elemental maps of Si and O for B370 show outlines of circles similar to those of Cd and S, but with wider diameters and greater thicknesses. This suggests again that some of silica dissolved during the HF etching process has been precipitated along the inner and outer surfaces of the CdS shell.

3.4.2. Further Characterization. The HRXRD spectra of Figure 3-5 also confirm the cubic crystallinity of CdS nanobubbles B300, B370, and B400. Using the

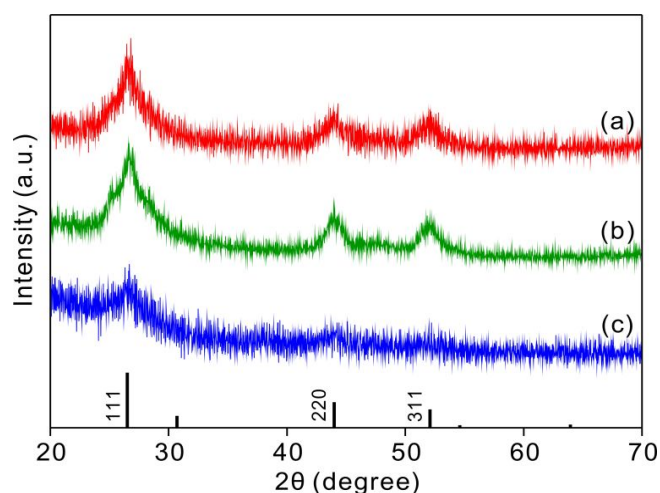


Figure 3-5. HRXRD spectra of CdS nanostructures B300 (a), B370 (b), and B400 (c), revealing the (111), (220), and (311) lattice planes of the cubic zinc blende CdS crystal structure (reference shown at the bottom, JPCDS Card No. 04-008-8227).

Scherrer equation²⁶ and assuming that peak broadening arises entirely from size effects, we have calculated the average crystallite sizes: 3.4 ± 0.1 nm (B300), 3.4 ± 0.2 nm (B370), and 3.6 ± 0.2 nm (B400). The small and uniform crystallite sizes also indicate that our CdS nanobubbles have good crystallinity.

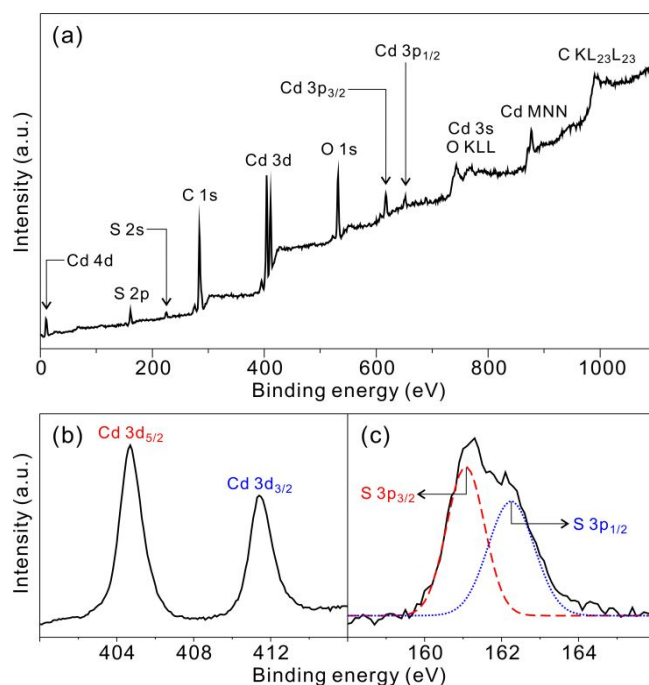


Figure 3-6. Complete survey (a), Cd 3d (b), and S 2p (c) XPS spectra of CdS nanobubbles B370. The S 2p_{3/2} and 2p_{1/2} curves have been deconvoluted from Gaussian fitting.

The XPS spectra of B370 provide further insight regarding the composition of CdS nanobubbles (Figure 3-6). Binding energies (E_B) have been corrected for specimen charging by referencing the C 1s peak to 284.5 eV.²⁷ The complete survey spectrum shows that besides Cd and S elements, the O element also exists noticeably.

O ($E_B(1s) = 532.1$ eV) was detected from SiO_2 ($E_B(\text{O } 1s) = 533.0$ eV)²⁸ particles remaining after etching and from O_2 molecules adsorbed on the surface of the CdS nanobubbles. The peak energies of 404.7 eV (Cd $3p_{5/2}$) and 411.4 eV (Cd $3p_{3/2}$) correspond relatively well to the literature E_B values of 405.0 eV and 411.7 eV,²⁹⁻³¹ respectively. The XPS spectrum of S 2p has been deconvoluted into two Gaussian bands with E_B values of 161.1 eV (S $2p_{3/2}$) and 162.2 eV (S $2p_{1/2}$), which also correspond well with the respective literature values of 161.4 eV and 162.6 eV.²⁹⁻³¹ The Cd/S atomic ratio of 1.3 obtained from the XPS data agrees very well with that of 1.3 from the EDX data of Figure 3-4. The Cd/S atomic ratio larger than 1, as well as the observed down-shifted E_B values of Cd 3d and S 3p, is considered to suggest that the majority of defects in CdS nanobubbles are due to anion vacancies.

The extinction and PL spectra of B370 in Figure 3-S3 in section 3.7 give us an interesting insight on the photophysical properties of CdS nanobubbles. CdS nanobubbles absorb a wide range of light, from UV to the visible, which is imperative for use as a photocatalyst. The extinction spectra of CdS nanobubbles have been used for modified Kubelka-Munk plots³² to determine the band-gap energies of 2.62 ± 0.04 eV (B300), 2.60 ± 0.05 eV (B370), and 2.58 ± 0.02 eV (B400). Using the Brus equation³³⁻³⁴ and the band gaps, we have estimated the average crystallite sizes of individual samples: 4.8 ± 1.0 nm (B300), 5.0 ± 1.5 nm (B370), and 5.2 ± 0.7 nm (B400). The shoulder peak in the modified Kubelka-Munk plot of Figure 3-S3 has been assigned to the surface-state band gap created by the well-known sulfur vacancies (2.2 eV).³⁵ Also, it is interesting to note that CdS nanobubbles exhibit a PL spectrum

with anti-Stokes shift as well as Stokes shift. This is due to quantum confinement-induced valence-band splitting, which has already been reported in detail.³⁶

3.4.3. Formation Mechanism. CdS nanobubbles with a uniform shell thickness have been prepared successfully as shown in Figure 3-1. TEOS undergoes a sol-gel process in the presence of various amounts of base catalysts, forming silica template nanospheres with narrow size distributions. Thereafter, the hydroxyl groups on the surfaces of silica nanospheres have been treated with APTES to functionalize the surfaces with amino groups. It has been reported²³ that the complete functionalization of the silica surfaces is a key factor for proper coating. Then, Cd²⁺ ions have been coordinated to the amino groups under stirring at 60 °C for 15 h to form an intermediate nanosphere with silica-supported nitrogenous cadmium complexes (SiO₂-NH₂-Cd²⁺). The Cd 3d_{5/2} peak (E_B = 404.7 eV) in the XPS data of intermediate nanospheres (Figure 3-S4 in section 3.7) indicates that Cd is present neither as elemental Cd (E_B = 405.0 eV)^{30, 37-38} nor as precursor CdCl₂ (E_B = 406.1 eV).^{30, 34} The XPS data also reveal that the Cd²⁺ cations have been coordinated to N atoms. The observed high E_B(1s) value of N at 399.1 eV, compared with the E_B(N 1s) of C₂H₅NH₂ at 398.4 eV,³⁹ suggests that each N atom is also bound to a highly electronegative O atom. The observed Cd/N atomic ratio of 2.3 suggests that other ligands are also coordinated to Cd²⁺ cations. Although the complete survey spectrum indicates the presence of Cl, the observed atomic ratio of Cl/Cd is much smaller than 2. Although the E_B(1s) value of O at 531.1 eV in Figure 3-S4 is greater than that for CdO at 528.6 eV, it is smaller than that for SiO₂ at 533.0 eV.⁴⁰ This suggests that a significant

fraction of O atoms are also present at the surface of the intermediate nanospheres to form complexes with Cd²⁺ ions.

The colloidal solution of intermediate nanospheres was subsequently centrifuged to dispose of any Cd²⁺ cations left in the solution, redispersed, and added with the sulfur source, Na₂S. After being stirred at room temperature for 1 h, the solution was subject to microwave irradiation for 10 min; the color of the dispersion changed from a white color with a just tint of yellow to bright yellow. Microwave irradiation has allowed for the rapid homogeneous nucleation of CdS nanoparticles along the surfaces of silica template nanospheres. After centrifugation and redispersion, produced SiO₂@CdS core@shell nanocomposites were etched with an excess amount of HF(aq) to remove the silica cores effectively *via* the stoichiometric reaction of SiO₂(s) + 4HF(aq) → SiF₄(g) + 2H₂O(l), although a small percentage of silica precipitated back onto the inner and outer surfaces of CdS nanobubbles during the washing process. Compared with a polystyrene template⁴¹ or template-free⁴² synthetic method of CdS hollow nanospheres, the above-mentioned preparation allows for greater control to result in highly uniform, well-defined hollow nanostructures with a very thin shell thickness. This fabrication has other advantages: it has very few steps, it provides control over the size of the nanobubbles, it is easily scalable, and it does not require an inert environment. It should be noted that although this method allows for very good control over size, CdS nanobubbles with diameters less than 50 nm were not able to be fabricated (Figure 3-S5 in section 3.7). Figure 3-S5b shows that complete CdS nanoshells were not produced on the surfaces of silica nanotemplates when the nanosphere sizes were too small.

3.4.4. Photocatalytic Performances. The photocatalytic properties of CdS nanobubbles have been explored by monitoring the time-dependent absorbance changes of RhB under irradiation by a Xe lamp. RhB is a highly photostable dye consisting of a central xanthene ring connected to four N-ethyl groups, two on each side. The concentration of RhB in the solution at a specific time has been estimated by monitoring the optical density, A , at the literature wavelength⁴³ of the RhB absorption maximum (554 nm). The initial RhB concentration, A_0 , is represented by the optical density at 554 nm of the RhB solution after the nanocatalysts have reached an adsorption-desorption equilibrium with RhB by being stirred in the dark for 1 h; RhB has been found to have low adsorption (< 1%) to any of the nanocatalysts mentioned in this work.

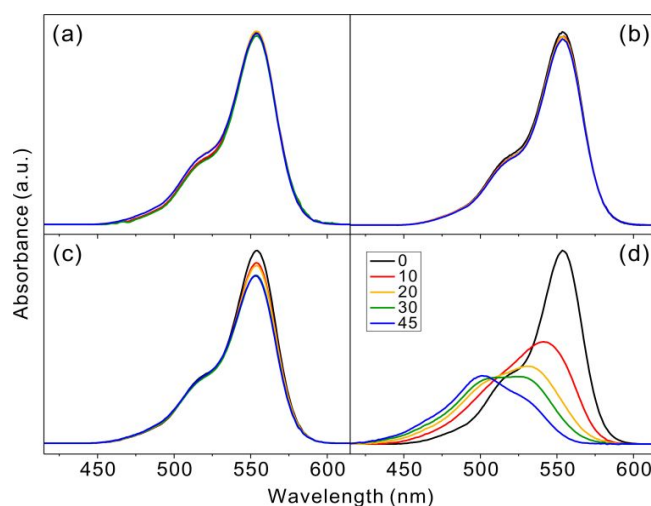


Figure 3-7. Baseline-modified absorption spectra of 10 μM RhB solutions in the presence of light without catalysts (a), in the absence of light with 0.1 g L^{-1} B300 (b), with light and 0.1 g L^{-1} C300 (c), and with light and 0.1 g L^{-1} B300 (d), measured at elapsed times indicated in the units of min.

The initial control experiments of Figure 3-7 reveal that both light irradiation and photocatalysts are vital components to the degradation of RhB. Less than 4% of RhB was decomposed in 45 min when either of these components was missing, but more than 96% of RhB was decomposed within the same time period in the presence of both 0.1 g L⁻¹ B300 and light irradiation. The photocatalytic performances of B300 CdS nanobubbles have been compared with those of C300 SiO₂@CdS core@shell nanocomposites under the same conditions. The concentration of RhB has decreased much faster by about 20 times in the presence of the CdS nanobubbles than in the presence of the core@shell nanocomposites. The absorption maximum of the B300-present solution exhibited hypsochromic shift from 554 nm (0 min) to 500 nm (45 min) as a result of the stepwise N-deethylation of RhB (see the section 3.5).

The pseudo-first-order degradation kinetic profiles of RhB *via* CdS nanophotocatalysts in the presence of light irradiation have been employed (Figure 3-8) to extract the degradation rate constants in Table 1 by using the linear plots of $\ln(A/A_0) = -kt$, where k is the rate constant and t is the time. Plots of $-\ln(A/A_0)$ *vs.* t for the photocatalytic degradation of RhB are shown with varying B300 concentrations (Figure 3-8a); as expected, k increases with concentration increase. In the inset, the variation of $\log k$ with $\log c$, where c represents the gram concentration of B300, has been fitted to yield a slope of 1.07 ± 0.05 : $k \propto c^{1.07}$. This demonstrates that the rate constant varies nearly linearly with the concentration, and that the concentrations of the CdS nanophotocatalysts are kept to be sufficiently low in our photocatalytic experiments. Furthermore, pseudo-first-order degradation profiles *via* B300, B370, and B400 have also been compared to study the size effects of the nanobubbles on k (Figure 3-8b).

The rate of degradation has been found to increase with decrease in the outer diameters (d) of the CdS nanobubbles. The inset in Figure 3-8b shows the variation of $\log k$ with $\log d$ for the CdS nanobubbles. The linearly fitted slope of the nanobubbles has been found to be -1.44 ± 0.39 : $k \propto d^{-1.44}$ (see below).

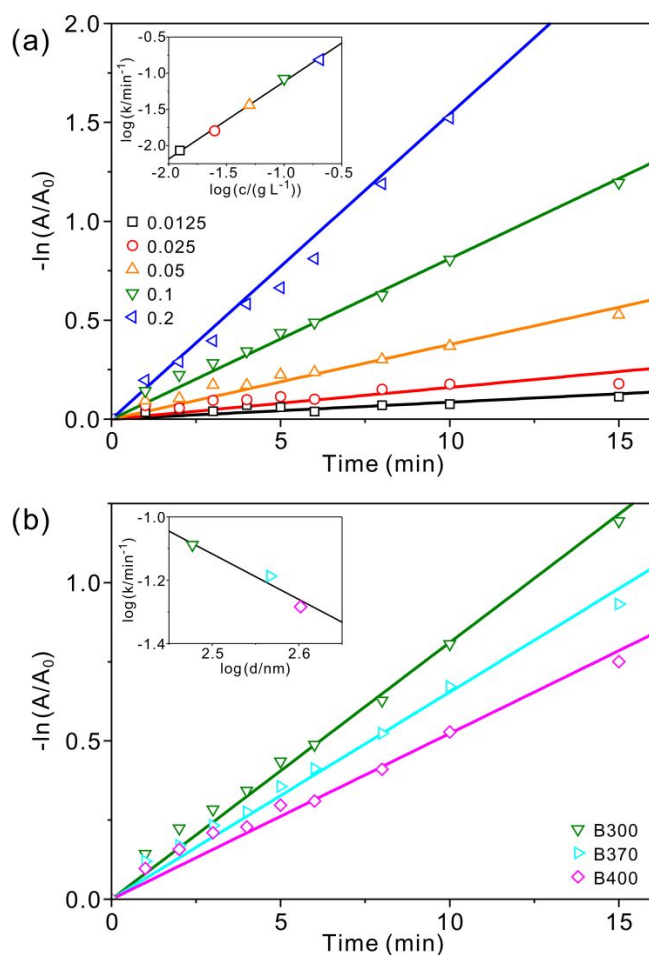


Figure 3-8. First-order kinetics, $-\ln(A/A_0)$ vs. t , for the catalytic degradation of $10 \mu\text{M}$ RhB(aq) via B300 CdS nanobubbles at various concentrations indicated in the units of g L^{-1} (a) and via B300, B370, and B400 CdS nanobubbles with varying nanobubble sizes (b) exposed to irradiation by a 300 W Xe lamp. The inset of panel a shows the variation of $\log k$ with $\log c$ while the inset of panel b shows the variation of $\log k$ with $\log d$.

Table 3-1. Rate constants (k) for the catalytic degradation of 10 μM RhB(aq) *via* CdS nanocatalysts under irradiation by a 300 W Xe lamp.

Nanocatalyst	Concentration (g L^{-1})	k (min^{-1})
^a	0.00	0.0005 ± 0.0007
B300	0.10	0.081 ± 0.002^b
B370	0.10	0.065 ± 0.002
B400	0.10	0.052 ± 0.002
C300	0.10	0.0044 ± 0.0011
C370	0.10	0.0014 ± 0.0004
C400	0.10	0.0012 ± 0.0005

^a In the absence of nanocatalysts. ^b The rate constant for the catalytic degradation of 10 μM RhB(aq) *via* 0.1 g L^{-1} B300 in the absence of light is $0.0011 \pm 0.0003 \text{ min}^{-1}$.

B300 CdS nanobubbles have shown enhanced photocatalytic performances also under irradiation by natural sunlight (Figure 3-S6 in section 3.7). The photocatalytic degradation rate of 20 μM RhB(aq) in the presence of 0.10 g L^{-1} B370 under natural sunlight has been observed to be $0.059 \pm 0.001 \text{ min}^{-1}$. This suggests indeed that CdS nanobubbles have high potential as an economically competitive photocatalyst in new solar-energy-harvesting advanced oxidation technologies.

3.4.5. Possible Photocatalytic Mechanism. As already shown in Figure 3-8a, the linear dependence of k on c may lead to suggest that the rate constant varies linearly with the nanophotocatalyst surface area. To further study the effects of the surface areas on the rate constants, the theoretical rate changes of S_O / V , the outer surface area per volume, and S_T / V , the total surface area per volume, with changes in diameters have been calculated for perfectly spherical CdS nanobubbles with uniform thicknesses; note that V is the volume of the CdS nanoshell. The total surface area is equal to the sum of the inner surface area (surface area of a sphere with $r = d / 2 - l$)

and the outer surface area (surface area of a sphere with $r = d / 2$). With $l = 11$ nm, the following equations have been derived:

$$\frac{S_O}{V} = \frac{6d^2}{d^3 - (d-22)^3} \quad (\text{nm}^{-1}) \quad (3-1)$$

$$\frac{S_T}{V} = \frac{6d^2 + 6(d-22)^2}{d^3 - (d-22)^3} \quad (\text{nm}^{-1}) \quad (3-2)$$

Using the above-mentioned equations, we have estimated S_O/V and S_T/V of thin CdS nanobubbles with varying diameters of 300, 370, and 400 nm. The theoretical dependence of $\log(S_O/V)$ on $\log d$ has been calculated to be -0.0656 while that of $\log(S_T/V)$ on $\log d$ has been calculated to -0.0015 . In other words, both S_O/V and S_T/V remain almost invariant regardless of d whereas k has been found to vary nonlinearly with the inverse of d ($k \propto d^{-1.44}$). This indicates that the rate constant depends hardly on the surface area of the nanobubbles, but varies with the size of the nanobubbles for a different reason, which we believe is due to the nanoreactor confinement effect of hollow-structured nanocatalysts.²⁰ CdS nanobubbles with smaller diameters exhibit greater rate constants, consistent with the trend for hollow nanocatalysts of the size range exhibiting the nanoreactor confinement effect.⁴⁴

The changes that occur in the UV/vis spectra during the degradation of RhB also give us information regarding the RhB degradation pathways. The hypsochromic shift of the RhB absorption maximum from 554 nm to 500 nm by photodegradation in the presence of CdS nanobubble catalysts is consistent with the sequential removal of the N-ethyl groups from the RhB molecule, where each N-deethylation results in a blue shift of the absorption maximum. Previous studies⁴⁵⁻⁴⁸ have stated that the N-deethylation process involves a primary step in which an electron from the nitrogen

atom of the excited singlet state of RhB ($E_0 = -1.09$ V vs. the normal hydrogen electrode (NHE))⁴⁹ is transferred to a CdS nanoparticle. The well-known intermediates have been identified as *N,N*-diethyl-*N'*-ethylrhodamine, *N*-ethyl-*N'*-ethylrhodamine (EER), *N,N*-diethyl-rhodamine (DR), *N*-ethylrhodamine, and rhodamine (R), where EER and DR are isomers of each other.^{46, 48-52} Using the peak absorbance of R at 500 nm and the molar extinction coefficients of RhB (11.5×10^4 M⁻¹ cm⁻¹) and R (8.4×10^4 M⁻¹ cm⁻¹),⁴⁵ it has been calculated that 47% of the initial RhB molecules remain in the solution as fully N-deethylated xanthenes structures. However, considering a previous report⁴⁹ of N-deethylation where > 90% of the xanthene-conjugated chromophores result from a large predomination of N-deethylation over the cleavage of the aromatic ring, we suggest that the N-deethylation and the cleavage of the conjugated ring compete with each other as the degradation pathways of RhB photocatalyzed *via* CdS nanobubbles. This evidence indicates that CdS nanobubbles photocatalyze both the rapid N-deethylation of RhB and the complete mineralization of RhB in general.

On the other hand, the absence of hypsochromic shifts in the absorption maximum indicates that only the direct destruction of the conjugated xanthene structure occurs during the photocatalytic degradation of RhB *via* SiO₂@CdS core@shell nanocomposites. The destruction process is facilitated by reactive oxygen species produced by photoexcited CdS nanocatalysts. For bulk CdS, electrons in the conduction band ($E_0 = -0.85$ V vs. NHE) have a reduction potential negative enough to reduce oxygen molecules to superoxide radicals ($O_2/O_2^{\cdot-}$; $E_0 = -0.33$ V vs. NHE) while the reduction potential of holes in the valence band ($E_0 = +1.55$ V vs. NHE) is not positive enough to overcome the reaction barrier to oxidize water molecules and

hydroxide ions into hydroxyl radicals ($\text{OH}\cdot, \text{H}^+/\text{H}_2\text{O}$; $E_0 = +2.73 \text{ V vs. NHE}$ and $\text{OH}\cdot/\text{OH}^-$; $E_0 = +1.90 \text{ V vs. NHE}$).^{12, 53-55} The production of superoxide radicals may be restricted by the rapid electron-hole recombination of CdS. The observed PL spectrum of Figure 3-S3 shows that electron-hole recombination occurs at higher-energy electron and hole states even at room temperature, suggesting extremely short lifetimes of electrons and holes which have been reported to be in the range of picoseconds.⁵⁶⁻⁵⁷ Because excited electrons have extremely short lifetimes in the conduction band, the chance of an electron migrating to an adsorbed O_2 molecule is low, ultimately resulting in a slower RhB degradation rate with the nanocomposite photocatalysts.

Photoexcitation of RhB does not contribute to photocatalysis *via* $\text{SiO}_2@\text{CdS}$ nanocomposites whereas that, as well as the photoexcitation of CdS, is effective in photocatalysis *via* CdS nanobubbles. Therefore, it can be concluded that the confining structure of CdS nanobubbles lowers the activation energy of the single-electron transfer pathway from RhB^* to CdS, which is known to be a surface-occurring reaction.⁴⁶ This can be attributed to the nanocage effect as discussed earlier. The inner surfaces of the nanobubbles have an increased number of active sites onto which RhB molecules are adsorbed. Because these sites are catalytically more active,¹⁹ an electron can be transferred from RhB^* to CdS easily. The dye radical cation, $\text{RhB}\cdot^+$, is then hydrolyzed to lose one ethyl group. The degradation of RhB *via* conjugated-ring attack has been compared for C300 and B300: 82% of RhB molecules remain after 45 min with nanocomposites while 47% of xanthenes rings remain with nanobubbles. Larger differences occur for the other remaining samples of different sizes. This signifies that

in addition to the adjunct of another degradation pathway (N-deethylation) for CdS nanobubbles, the degradation rate *via* the photocatalytic pathway of conjugated-ring attack also increases. It could be possible that adsorption of O₂ molecules occurs mostly on the inner cavity surfaces of the nanobubbles, resulting in build-up of reactive radicals within the cavities of the nanobubbles. Although RhB degradation *via* aromatic-ring attack is predominantly a solution bulk process,⁴⁶ the cavity sizes of hollow nanostructures control the collision rate between reactive oxygen species and RhB dye molecules.⁴⁴ Thus, it is suggested that the higher collision rate in smaller nanocavities also contributes to bring about the higher degradation rates of RhB with CdS nanobubbles with smaller sizes (Figure 3-8a).

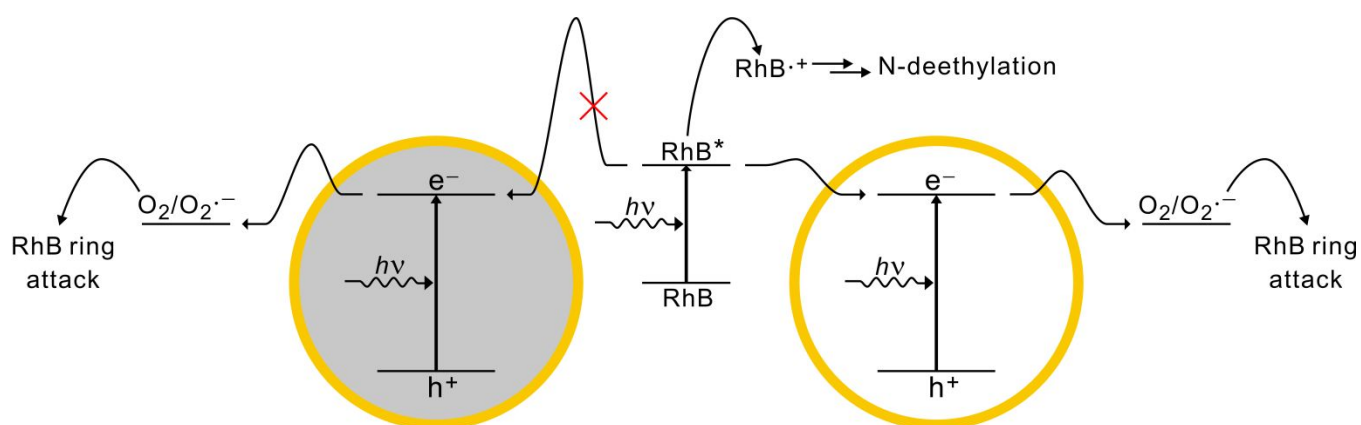


Figure 3-9. Proposed mechanisms for the photocatalytic degradation of RhB solutions *via* SiO₂@CdS core@shell composites (left) and CdS nanobubbles (right).

Figure 3-9 shows our proposed overall mechanisms schematically for the photocatalytic degradation of RhB(aq) in the presence of SiO₂@CdS core@shell

nanocomposites and CdS nanobubbles. Unlike the kinetic barrier *via* CdS nanobubbles, that for the single-electron transfer from RhB* is too high for the N-deethylation of RhB to occur *via* core@shell nanocomposites. It is believed that the lowering of the activation energy for this pathway with CdS nanobubbles is a direct result of the nanoreactor confinement enhancement. The simultaneous N-deethylation and conjugated-ring attack of RhB immensely enhance the photocatalytic degradation rate of RhB(aq) *via* CdS nanobubbles.

3.5. Conclusion

A novel fabrication method involving hard templates and microwave irradiation has been developed to synthesize size-controlled CdS nanobubbles with high photocatalytic activity. The CdS nanobubbles with diameters of 300, 370, and 400 nm have been found to consist of mostly cubic CdS nanocrystallites packed together into a shell with 11 nm thickness. The CdS nanobubbles efficiently photocatalyze the degradation of RhB *via* concurrent pathways of N-deethylation and direct conjugated-ring attack. These nanophotocatalysts have exhibited excellent photocatalytic performances under irradiation by a Xe lamp and under natural sunlight, showing high potential as low-cost sunlight-activated photocatalysts.

3.6. Acknowledgement

This work was supported by research grants from the National Research Foundation (NRF) of Korea (2011-0028981 and 2012-006345). D.J.J. is also thankful to the SRC program of NRF (2007-0056331).

3.7. Supporting Information

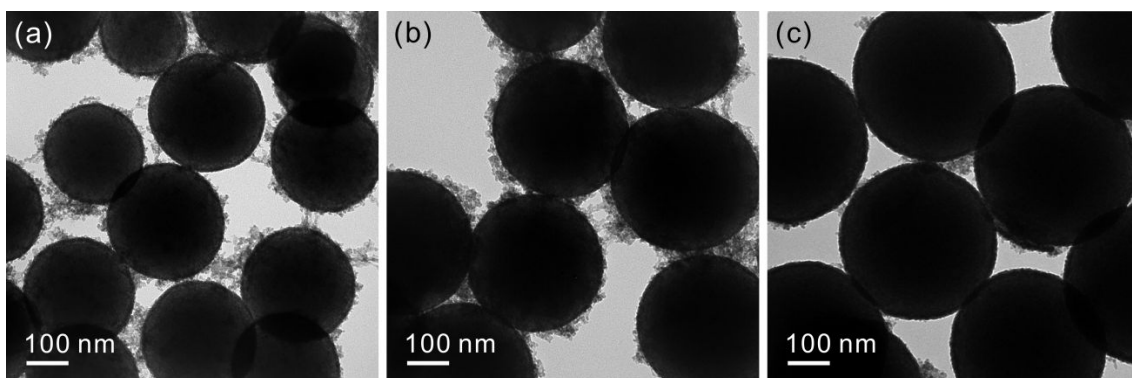


Figure 3-S1. TEM images of $\text{SiO}_2@\text{CdS}$ core@shell nanocomposites of different sizes: C300 (a), C370 (b), and C400 (c).

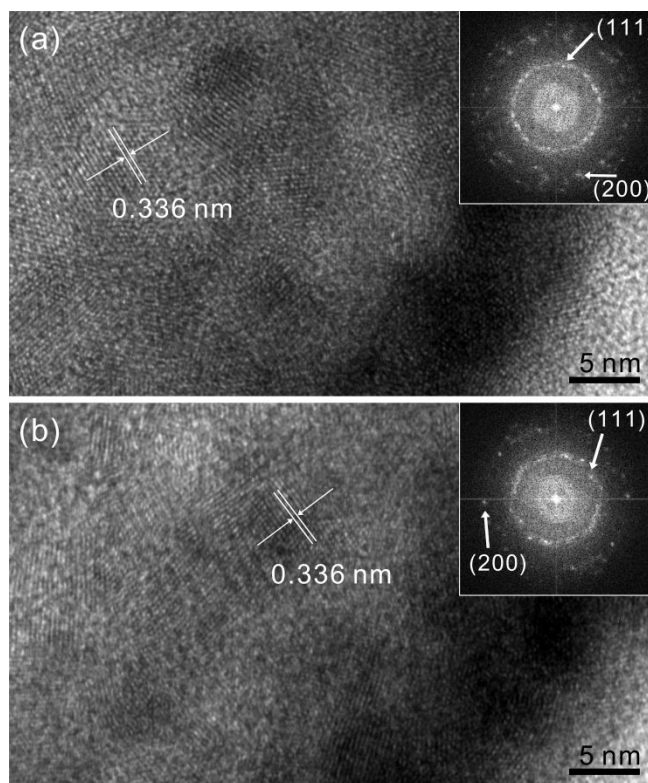


Figure 3-S2. HRTEM images of CdS nanobubbles B300 (a) and B400 (b) and their corresponding FFT patterns (insets).

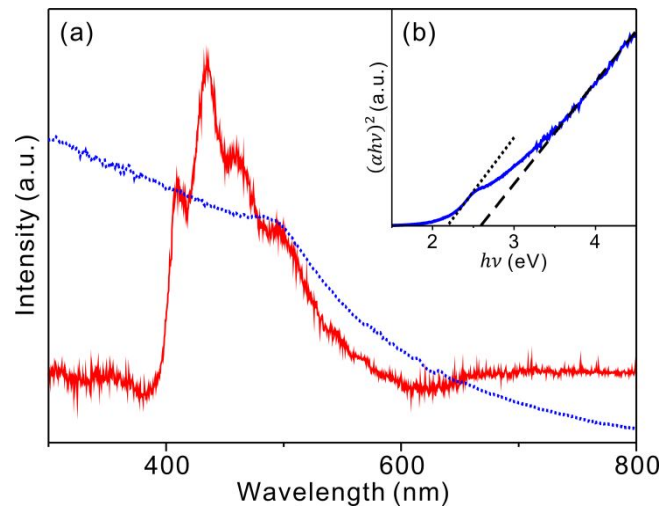


Figure 3-S3. Extinction (dotted) and PL, with excitation at 355 nm, (solid) spectra of B370 suspended in ethanol (a). $(\alpha h\nu)^2$ plots against $h\nu$ after removal of scattering (c/λ^4 , where c is an arbitrary constant) from the extinction spectrum to obtain the band gap of B370 (b). The intercept of the dashed line corresponds to the band gap of CdS nanobubbles while that of the dotted line corresponds to the energy gap created by sulfur-vacancy defects.

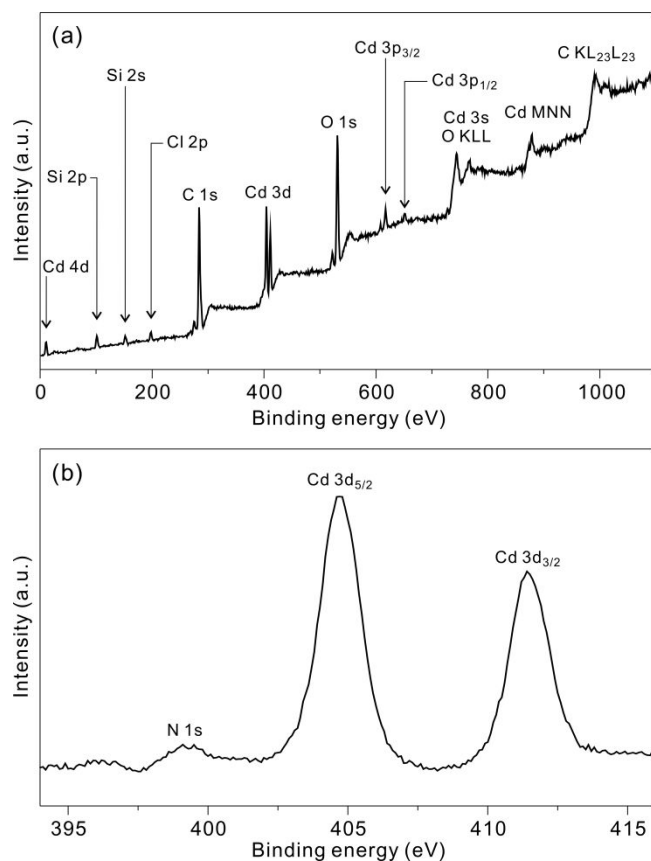


Figure 3-S4. Complete survey (a) and N 1s and Cd 3d close-up (b) XPS spectra of intermediate nanospheres with silica-supported nitrogenous cadmium complexes.

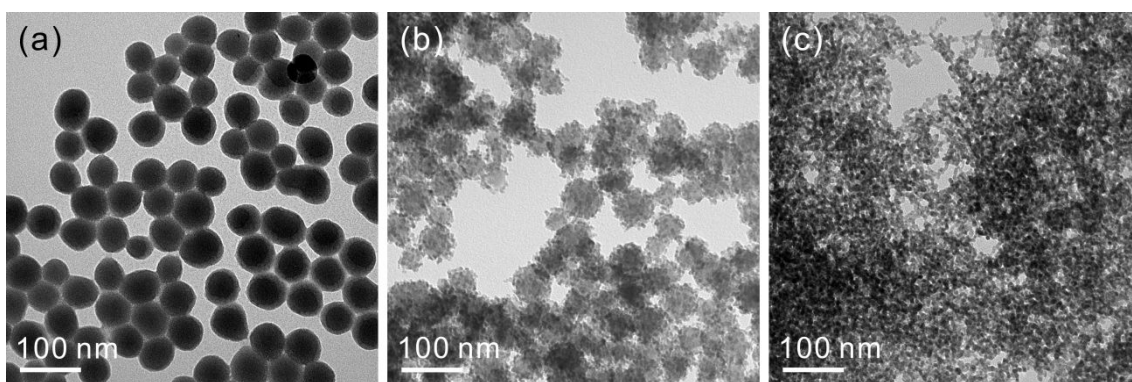


Figure 3-S5. TEM images showing SiO₂ core hard templates with 50 nm diameters (a), SiO₂@CdS core@shell composite structures with 60 nm diameters (b), and the product after etching (c).

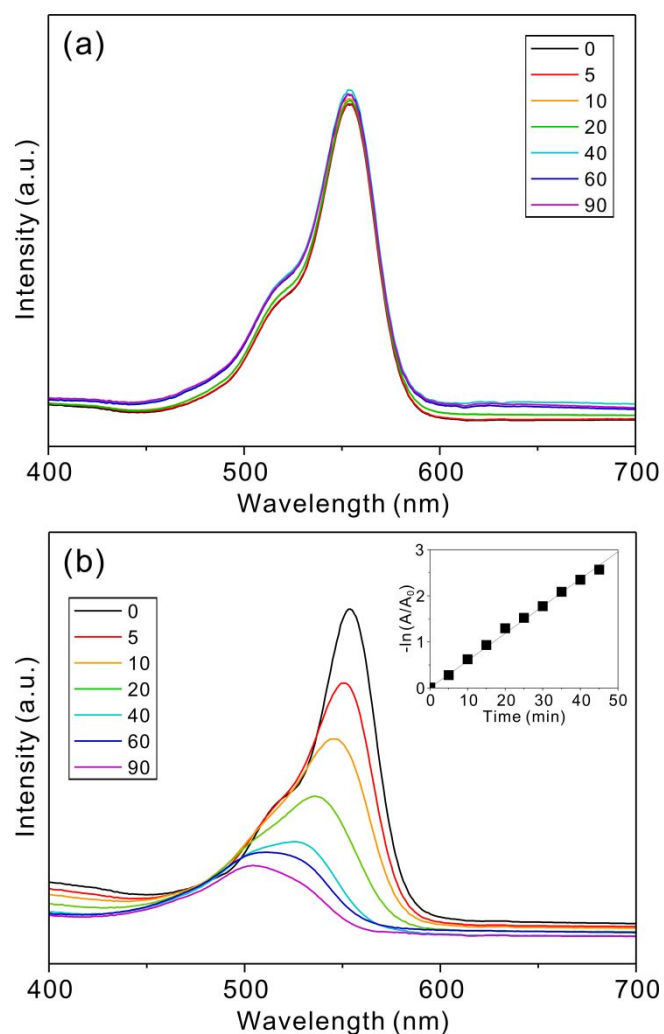


Figure 3-S6. Absorption spectra of 20 μM RhB aqueous solutions in the presence of natural sunlight without nanocatalysts (a) and with 0.10 g L^{-1} nanocatalyst B370 (b) measured at elapsed times indicated in the units of min. These experiments were carried out on a sunny fall day from 2 p.m. on the 24th of September in Seoul, Korea, where the maximum temperature of the day was 27 $^{\circ}\text{C}$ and the minimum was 17 $^{\circ}\text{C}$. The plot of $-\ln(A/A_0)$ vs. t , shown in the inset, has yielded a degradation rate constant of $0.059 \pm 0.001 \text{ min}^{-1}$.

3.8. References

- (1) H. Zhou, Y. Qu, T. Zeid, X. Duan. *Energy Environ. Sci.* **2012**, *5*, 6732-6743.
- (2) T. K. Townsend, N. D. Browning, F. E. Osterloh. *ACS Nano* **2012**, *6*, 7420-7426.
- (3) Z. Liu, W. Hou, P. Pavaskar, M. Aykol, S. B. Cronin. *Nano Lett.* **2011**, *11*, 1111-1116.
- (4) L. Liu, H. Zhao, J. M. Andino, Y. Li. *ACS Catal.* **2012**, *2*, 1817-1828.
- (5) Z. Chen, S. Liu, M.-Q. Yang, Y.-J. Xu. *ACS Appl. Mater. Interfaces* **2013**, *5*, 4309-4319.
- (6) D. S. Bhatkhande, V. G. Pangarkar, A. ACM Beenackers. *J. Chem. Technol. Biotechnol.* **2002**, *77*, 102-116.
- (7) L. Shi, P. Yin, Y. Dai. *Langmuir* **2013**, *29*, 12818-12822.
- (8) Z. Shu, X. Jiao, D. Chen. *CrystEngComm* **2013**, *15*, 4288-4294.
- (9) G. Liu, S. Liang, W. Wu, R. Lin, N. Qing, R. Liang, L. Wu. *Nanotechnology* **2013**, *24*, 255601-255609.
- (10) J. Lee, K. Han, D.-J. Jang. *Appl. Catal., A* **2014**, *469*, 380-386.
- (11) C. Chen, W. Ma, J. Zhao. *Chem. Soc. Rev.* **2010**, *39*, 4206-4219.
- (12) H. Kisch. *Angew. Chem. Int. Ed.* **2013**, *52*, 812-847.
- (13) P. V. Kamat. *Chem. Rev.* **1993**, *93*, 267-300.
- (14) S. H. S. Chan, T. Yeong Wu, J. C. Juan, C. Y. Teh. *J. Chem. Technol. Biotechnol.* **2011**, *86*, 1130-1158.
- (15) U. I. Gaya, A. H. Abdullah. *J. Photochem. Photobiol., C* **2008**, *9*, 1-12.

- (16) J. Cao, J. Z. Sun, J. Hong, H. Y. Li, H. Z. Chen, M. Wang. *Adv. Mater.* **2004**, *16*, 84-87.
- (17) Q. Li, B. Guo, J. Yu, J. Ran, B. Zhang, H. Yan, J. R. Gong. *J. Am. Chem. Soc.* **2011**, *133*, 10878-10884.
- (18) Y. Zhang, N. Zhang, Z.-R. Tang, Y.-J. Xu. *Chem. Sci.* **2012**, *3*, 2812-2822.
- (19) M. A. Mahmoud, R. Narayanan, M. A. El-Sayed. *Acc. Chem. Res.* **2013**, *46*, 1795-1805.
- (20) M. A. Mahmoud, F. Saira, M. A. El-Sayed. *Nano Lett.* **2010**, *10*, 3764-3769.
- (21) M. A. Mahmoud, M. A. El-Sayed. *Nano Lett.* **2011**, *11*, 946-953.
- (22) J. B. Joo, I. Lee, M. Dahl, G. D. Moon, F. Zaera, Y. Yin. *Adv. Funct. Mater.* **2013**, *23*, 4246-4254.
- (23) J.-A. Kwak, D. K. Lee, D.-J. Jang. *Appl. Catal., B* **2013**, *142-143*, 323-328.
- (24) W.-W. So, J.-S. Jang, Y.-W. Rhee, K.-J. Kim, S.-J. Moon. *J. Colloid Interface Sci.* **2001**, *237*, 136-141.
- (25) W. Stöber, A. Fink, E. Bohn. *J. Colloid Interface Sci.* **1968**, *26*, 62-69.
- (26) J. I. Langford, A. J. C. Wilson. *J. Appl. Crystallogr.* **1978**, *11*, 102-113.
- (27) Y. Kim, D.-J. Jang. *RSC Adv.* **2013**, *3*, 16945-16948.
- (28) T. L. Barr. *Appl. Surf. Sci. (1977-1985)* **1983**, *15*, 1-35.
- (29) V. G. Bhide, S. Salkalachen, A. C. Rastog, C. N. R. Rao, M. S. Hegde. *J. Phys. D: Appl. Phys.* **1981**, *14*, 1647-1656.
- (30) J. Chastain, R. C. King, J. F. Moulder. *Handbook of x-ray photoelectron spectroscopy : a reference book of standard spectra for identification and interpretation of XPS data*; Physical Electronics: Eden Prairie, Minnesota, 1995.

- (31) M. Marychurch, G. C. Morris. *Surf. Sci.* **1985**, *154*, L251-L254.
- (32) L. Li, Y.-W. Yang, G.-H. Li, L.-D. Zhang. *Small* **2006**, *2*, 548-553.
- (33) H. Y. Acar, R. Kas, E. Yurtsever, C. Ozen, I. Lieberwirth. *J. Phys. Chem. C* **2009**, *113*, 10005-10012.
- (34) L. E. Brus. *J. Chem. Phys.* **1984**, *80*, 4403-4409.
- (35) Q. Xiao, C. Xiao. *Appl. Surf. Sci.* **2009**, *255*, 7111-7114.
- (36) Y. Kim, D.-J. Jang. *Chem. Commun.* **2013**, *49*, 8940-8942.
- (37) C. D. Wagner. *Faraday Discuss. Chem. Soc.* **1975**, *60*, 291-300.
- (38) R. I. Hegde, S. R. Sainkar, S. Badrinarayanan, A. P. B. Sinha. *J. Electron. Spectrosc. Relat. Phenom.* **1981**, *24*, 19-25.
- (39) M. Barber, J. A. Connor, M. F. Guest, I. H. Hillier, M. Schwarz, M. Stacey. *J. Chem. Soc., Faraday Trans. 2* **1973**, *69*, 551-558.
- (40) J. S. Hammond, S. W. Gaarenstroom, N. Winograd. *Anal. Chem.* **1975**, *47*, 2193-2199.
- (41) Y. Wang, G. Wang, H. Wang, C. Tang, Z. Jiang, L. Zhang. *Chem. Lett.* **2007**, *36*, 674-675.
- (42) G. Lin, J. Zheng, R. Xu. *J. Phys. Chem. C* **2008**, *112*, 7363-7370.
- (43) H. Gnayem, Y. Sasson. *ACS Catal.* **2013**, *3*, 186-191.
- (44) C. W. Yen, M. A. Mahmoud, M. A. El-Sayed. *J. Phys. Chem. A* **2009**, *113*, 4340-4345.
- (45) T. Watanabe, T. Takizawa, K. Honda. *J. Phys. Chem.* **1977**, *81*, 1845-1851.
- (46) T. Wu, G. Liu, J. Zhao, H. Hidaka, N. Serpone. *J. Phys. Chem. B* **1998**, *102*, 5845-5851.

- (47) T. Takizawa, T. Watanabe, K. Honda. *J. Phys. Chem.* **1978**, *82*, 1391-1396.
- (48) C. Chen, W. Zhao, P. Lei, J. Zhao, N. Serpone. *Chem. Eur. J.* **2004**, *10*, 1956-1965.
- (49) X. Hu, T. Mohamood, W. Ma, C. Chen, J. Zhao. *J. Phys. Chem. B* **2006**, *110*, 26012-26018.
- (50) J. Yang, C. Chen, H. Ji, W. Ma, J. Zhao. *J. Phys. Chem. B* **2005**, *109*, 21900-21907.
- (51) Z. He, S. Yang, Y. Ju, C. Sun. *Journal of Environmental Sciences* **2009**, *21*, 268-272.
- (52) Y. Bessekhoud, N. Chaoui, M. Trzpit, N. Ghazzal, D. Robert, J. V. Weber. *J. Photochem. Photobiol., A* **2006**, *183*, 218-224.
- (53) S. B. Rawal, S. Bera, D. Lee, D.-J. Jang, W. I. Lee. *Catal. Sci. Technol.* **2013**, *3*, 1822-1830.
- (54) P. Wardman. *J. Phys. Chem. Ref. Data* **1989**, *18*, 1637-1755.
- (55) C. C. Winterbourn. *Nat. Chem. Biol.* **2008**, *4*, 278-286.
- (56) S. Logunov, T. Green, S. Marguet, M. A. El-Sayed. *J. Phys. Chem. A* **1998**, *102*, 5652-5658.
- (57) J. K. Cooper, J. Cao, J. Z. Zhang. *ACS Appl. Mater. Interfaces* **2013**, *5*, 7544-7551.

Appendices

A.1. Stöber Method

In the synthesis of silica hard templates, SiO₂ core structures were produced *via* the one-step Stöber method.¹ From tetraethyl orthosilicate (TEOS), metal-oxide oxo-bridges form with Si as the metal, ultimately resulting in nucleation of SiO₂ spheres (Figure A-1). The size of the colloids may be controlled by various approaches. A higher concentration of TEOS results in larger spheres; a dilution of the overall mixture with water results in smaller spheres; a longer reaction time results in larger spheres; use of a different alcoholic solvent changes sphere sizes (methanol < ethanol < n-butanol; where methanol results in the smallest sphere and n-butanol results in the largest sphere); and a higher concentration of ammonia(aq) results in larger spheres. Because changes in ammonia concentration result in the largest change in size, sizes of the silica hard templates in this dissertation have been controlled by changing the amount of ammonia(aq) added.

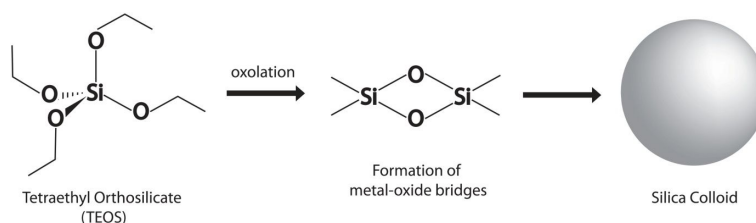


Figure A-1. Schematic of the sol-gel condensation of TEOS in the formation of silica colloidal spheres.

¹ W. Stöber, A. Fink, E. Bohn. *J. Colloid Interface Sci.* **1968**, 26, 62-69.

A.2. Scherrer Equation

For crystallites less than 100 nm, the Scherrer equation can be used to estimate the average size of crystallites in the sample. The Scherrer equation assumes that all broadenings of the X-ray peaks in the X-ray diffraction (XRD) data arise from size factors. The Scherrer equation¹ is given by:

$$\tau = \frac{K\lambda}{\beta \cos \theta} \quad (\text{A-1})$$

where τ is the mean size of the crystalline domains, K is the shape factor, λ is the X-ray wavelength, β is the full-width at half-maximum of the XRD peak, and θ is the Bragg angle.

The mean crystallite sizes in sections 2.4 and 3.4 have been calculated by estimating K to 0.94,² which is a theoretical estimate for spherical cubic nanocrystallites. The X-ray diffractometer used for measurements operates with a Cu $K_{\alpha 1}$ X-ray beam with λ equal to 0.154056 nm. The line broadening, β , was measured for the (111) peak, with $\theta = 13.30^\circ$, due to its high intensity.

It is important to realize that the Scherrer formula provides an estimate for the smallest possible particle size, since all broadening is assumed to arise from size effects. Some of the broadening may be contributed to other factors such as instrumental effects, inhomogeneous strain, and crystal lattice defects. To account for these factors and obtain a better estimate of the crystallite size, a more in-depth

¹L. A. Patterson. *Phys. Rev.* **1939**, 56, 978.

²J. I. Langford, A. J. C. Wilson. *J. Appl. Cryst.*, **1978**, 11, 102.

analysis is required. In the studies carried out in this thesis, only simple calculations have been made with the Scherrer equation, which may be a reason to the discrepancies in CdS nanoparticle size estimates.

A.3. Brus Equation

When the band gap of a homogeneous nanosphere is known, the band gap of the nanoparticle (NP) may be used to determine the size of the NP by using the Brus equation¹ as listed below:

$$\Delta E_g = E_g(QD) - E_g(bulk) = \left(\frac{\hbar^2 \pi^2}{2R^2}\right) \left(\frac{1}{m_e} + \frac{1}{m_h}\right) - 1.8 \left(\frac{e^2}{4\pi\epsilon\epsilon_0 R}\right) \quad (\text{A-2})$$

where \hbar is the reduced Planck constant (6.582119×10^{-16} eV·s), R is the radius of the NP, m_e is the effective mass of the electron, m_h is the effective mass of the hole, e is the elementary charge, ϵ is the dielectric constant of the solid, and ϵ_0 is the permittivity of a vacuum.

When the Brus equation was used in sections 2.4 and 3.4 in this thesis, calculations have been made by using constants from literature.² For CdS, $m_e = 0.3m_0$ and $m_h = 0.8m_0$ where m_0 is the reduced mass of an electron (9.11×10^{-31} kg), and $\epsilon_{Cds} = 5.7$. It should be noted that the Brus equation allows for a rather simple approximation of the NP size because it does not consider the coupling constant, μ , meaning that it does not consider the effects of valence band splitting.

¹L. E. Brus. *J. Chem. Phys.* **1984**, *80*, 4403.

²H. Y. Acar, *J. Phys. Chem. C.* **2009**, *113*, 10005.

A.4. Theoretical Fittings of Line-Scanned EDX Profiles: Core@Shell and Hollow Spheres

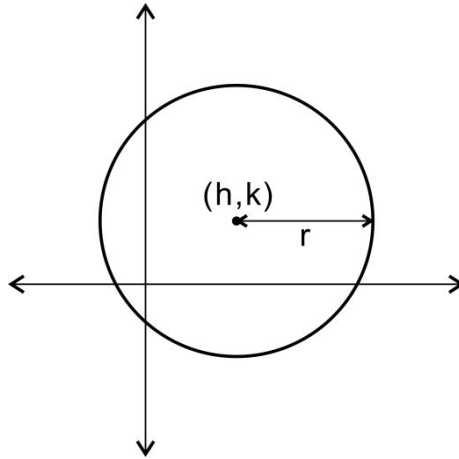


Figure A-2. A circle with center (h,k) and a radius r as described by eq. A-3.

The line-scanned EDX profiles in Figure 3-4 have been theoretical fitted by utilizing the fact that the cross-section of a sphere is a circle and that of a hollow sphere is a hollow circle. Equations A-5 and A-11, which were used for the fittings (see below), have been derived by manipulating the equation of a circle as shown in Figure A-2:

$$(x - h)^2 + (y - k)^2 = r^2 \quad (\text{A-3})$$

Setting $k = 0$, $h = x_0 + r$, and $r = d/2$, where $x_0 =$ distance between the origin and the sphere edge and $d =$ diameter, the following equation is obtained:

$$y = \sqrt{d(x - x_0) - (x - x_0)^2} \quad (\text{A-4})$$

Multiplying y by a constant, C , we get the number of counts, I , of diffracted x-rays in a line scan of a filled spherical particle along x , where x = distance or position:

$$I = C \{d(x - x_0) - (x - x_0)^2\}^{1/2} \quad (\text{A-5})$$

Intensity for a hollow sphere can be obtained by subtracting two circles with the same center but different radii, r_1 and r_2 , where $r_1 > r_2$:

$$y_1 = \sqrt{r_1^2 - (x - h)^2} \quad (\text{A-6})$$

$$y_2 = \sqrt{r_2^2 - (x - h)^2} \quad (\text{A-7})$$

Subtracting, eq. A-7 from eq. A-6, we get:

$$y_1 - y_2 = \sqrt{r_1^2 - (x - h)^2} - \sqrt{r_2^2 - (x - h)^2} \quad (\text{A-8})$$

Defining $h = x_0 + r_1$ and $r_2 = r_1 - t_{shell}$, the equation now becomes:

$$y_1 - y_2 = \sqrt{r_1^2 - (x - x_0 - r_1)^2} - \sqrt{(r_1 - t_{shell})^2 - (x - x_0 - r_1)^2} \quad (\text{A-9})$$

Finally, defining the outer diameter, $d = 2r_1$, the first part of the equation becomes the same as eq. A3-2, and the entire equation becomes as follows:

$$y_1 - y_2 = \sqrt{d(x - x_0) - (x - x_0)^2} - \sqrt{d(x - x_0 - t_{shell}) - (x - x_0)^2 + (t_{shell})^2} \quad (\text{A-10})$$

Multiplying $(y_1 - y_2)$ by a constant, we get the number of counts of diffracted x-rays in a line scan of a hollow spherical particle:

$$I = C [\{d(x - x_0) - (x - x_0)^2\}^{1/2} - \{d(x - x_0 - t_{shell}) - (x - x_0)^2 + (t_{shell})^2\}^{1/2}] \quad (\text{A-11})$$

Equation A3-3 can be used to estimate the shape of a line-scanned EDX profile of a particle with a circular cross-section, such as a sphere or cylinder. Both eq. A-5

and A-11 must be used to estimate the shape of a line-scanned EDX profile of a particle with a hollow circle cross-section, such as a hollow sphere or hollow cylinder. For hollow circular cross-sections, eq. A-5 must be used when $x_0 \leq x \leq (x_0 + t_{shell})$ and $(x_0 + d - t_{shell}) \leq x \leq (x_0 + d)$ and eq. A-11 must be used when $(x_0 + t_{shell}) < x < (x_0 + d - t_{shell})$.

For core@shell structures, eq. A3-3 can be used for the core shape along with eq. A-5 and A-11 for the shell such that $d_{core} + 2t_{shell} = d_{shell,outer}$ to approximate intensity profiles for a shell that is coated directly on top of the spherical core.

The terms, C , d , x_0 , and t_{shell} are variables that need to be estimated for the fitting.

A.5. List of Publications

1. **Younshin Kim** and Du-Jeon Jang, “Direct Observation of Valence Band Splitting Using Room Temperature Photoluminescence of CdS Hollow Submicrospheres,” *Chem. Commun.* **2013**, 49, 8940.

A.6. List of Presentations

A.6.1. International Presentations

1. **Younshin Kim**, Hyung-Bae Kim, Jin-Ah Kwak, and Du-Jeon Jang, “Microwave-Assisted Preparation of CdS Hollow Nanospheres with Enhanced Photocatalytic Activity,” *The First International Conference on Photocatalysis and Solar Energy Conversion: Development of Materials and Nanomaterials*, Daejeon, Korea (2012).

A.6.2. Domestic Presentations

1. **Younshin Kim**, Hyung-Bae Kim, and Du-Jeon Jang, “Facile Synthesis of Colloidal and Hollow CdS Nanospheres via Microwave Irradiation,” *The 109th Spring Meeting of the Korean Chemical Society*, Goyang, Korea (2012).
2. **Younshin Kim**, Hyung-Bae Kim, and Du-Jeon Jang, “Photocatalytic Enhancement of CdS Hollow Nanospheres Prepared via Microwave Irradiation,” *The 110th Summer Meeting of the Korean Chemical Society Physical Chemistry Subcommittee*, Sokcho, Korea (2012).
3. **Younshin Kim**, Hyung-Bae Kim, and Du-Jeon Jang, “Novel Photophysical Properties of CdS Hollow Submicrospheres Prepared via Microwave Irradiation,” *The 110th Autumn Meeting of the Korean Chemical Society*, Busan, Korea (2012).

4. **Younshin Kim** and Du-Jeon Jang, “Direct Observation of Valence Band Mixing in CdS Hollow Submicrospheres Prepared by Microwave Irradiation,” *The 111th Spring Meeting of the Korean Chemical Society*, Goyang, Korea (2013).

Abstract (Korean)

직경은 미세 마이크로미터 범위에 속하고 셀 두께는 양자구속 범위에 속하는 속이 빈 황화카드뮴 나노방울을 생성하는데 단단한 실리카 템플릿과 마이크로파 조사를 이용한 새로운 합성방법이 적용되었다. 그 황화카드뮴 나노방울은 독특한 광물리적 속성과 우수한 광촉매 작용을 보여주었다.

이 논문에서 언급되는 주제의 간단한 개요를 1 장에서 볼 수 있다. 반도체 나노입자들이 양자구속 범위에 속할 정도로 충분히 작을 때는 크기가 큰 물질들과는 광물리적 속성들이 달라진다. 나노입자의 합성방법들에 대한 일반적인 요약과 크기와 모양, 조화가능성의 중요함이 보여진다. 또한, 불균일 광촉매작용에서 나노반응기 구속효과가 나타나는 속 빈 할로우 나노구조들의 역할들이 서술되고 있다.

2 장에서는 황화카드뮴 나노방울들의 특이한 광물리적 특성에 대해 논하였다. 황화카드뮴 나노방울들은 양자구속 범위 내의 셀 두께로 합성되어 원자가 전자대 분열로 귀착되었다. 상온에서 이러한 현상들의 직접적인 관찰이 Chemical Communication 에 Communication report 를 통해 처음 보고되었다. 광루미네선스 스펙트럼들로부터 관찰된 데이터는 기존의 이론적 연구와 비교하여 해석되었다. 전자대에서의 나노입자 크기의 민감함, 분열 규모, 전이의 진동자 강도들 그리고 측정되고 비교된 전자/정공 상태 밀도 등을 논하고 있다.

3 장은 황화카드뮴의 합성, 특성 그리고 광촉매 적용에 초점을 두었다. 단단한 실리카 템플릿과 마이크로파 조사를 사용한 황화카드뮴 나노방울의 단계적 합성이

다른 크기의 명확한 구조를 가진 황화카드뮴 나노방울들을 산출하는데 집중되었다. 산출된 황화카드뮴 나노방울들은 투과전자현미경, 에너지 분산형 엑스선 분광기, 고해상도 엑스선 회절, 엑스선 광전자 분광법, 그리고 광분광학 연구를 통해 특성을 완전히 밝혀냈다. 황화카드뮴 나노방울의 광촉매 작용은 로오다민 B의 분열을 통해 검토되었다. 황화카드뮴 나노방울의 유사일차분해속도 상수는 나노반응기 구속효과 때문에 SiO₂@CdS 코어셸 나노복합재 보다 약 20 배 상승하는 것을 보여준다. 이 활성증대는 새로운 반응경로의 (N-deethylation) 활성화 에너지 감소와 본래의 반응경로 (방향족 고리 공격) 또한 빠르게 하여 이루어졌다.

주요어: 황화카드뮴, 속이 빈 나노스피어, 코어셸 나노스피어, 마이크로파 합성, 양자구속효과, 광촉매 작용, 나노반응기 구속효과

학번: 2012-20269

Acknowledgement

I would like to first and foremost express my sincere gratitude to my advisor, Professor Du-Jeon Jang, for his continuous guidance and support throughout my MSc. program at Seoul National University. He has been my mentor every step of the way during this two-year program, from the development of the ideas for this thesis to correcting tedious grammar mistakes. Professor Jang has not only helped me grow academically and professionally, but also helped me adjust to a new cultural environment by always taking the time to patiently explain cultural etiquettes.

I would also like to thank Professor Heon Kang and Professor YounJoon Jung for taking time off their busy schedules to be a part of my thesis committee. I have always looked up to them as professors of physical chemistry, and will continue to look forward to their future works.

I am also greatly in debt to my colleagues here at Nanostructure Fabrication Laboratory. I have learned so much from and look up to precedent graduates, 오훈선배, 영신오빠, 혁이오빠, 선영언니, 종엽오빠, 지영언니, 진아언니, as well as current Ph.D. candidates, 동기오빠, 연호오빠, 형배오빠. Thank you and congratulations to other graduates, 대기오빠, 명희언니. Also, I would like to express my thanks to 재원오빠, 다연언니, 혜리언니, for always lending a helping hand. I will continue to cheer you all on in your future endeavors.

I am also very grateful to 효진언니 for always being so supportive and caring, despite being members of different labs. I would also like to thank 재훈오빠, the only other UCL alumni here at SNU, who has always gone out of his way to look after me.

Special thanks also go out to all the friends and family that have supported me throughout my studies at SNU. High school friends from KIS, Ted Kim and Stephen Kim, are like actual brothers to me that I can always rely on. Christina Kang, thank you for being my lab-rat/nerd buddy. Thank you, Susie Youn, for being so adorable. Friends from London, Joon Choi, Joohyung Jeon, Sungeun Kim, Jayoung Kang, Sujin Kwon, and Chaeree Park, have patiently put up with all my whining and complaining. Thank you, Jin Lee and Sungkyun Park, for taking the time to visit me at school and encourage me in my studies. My life-long coaches, Mr. Jason Watanabe, Mr. Paul Perron, and Mr. Kori Sickles, who have coached me in cross country and basketball throughout high school, still continue to coach me through the ups and downs of life. Of course, I cannot leave out my favorite ladies, Sera Kim, Phoebe Min, Kena Park, Youshin Song, and Ellie Sul, who have always been there for me despite the fact that they are all scattered around the world. You know I love each and every one of you to death and that I wouldn't have been able to withstand life in Korea without all your love and support.

And lastly, I would like to thank my family. It has been an honor for me to attend and learn at the exact school where my father has received his degrees; it means a lot to me that we are now alumni to the same school. I would like to thank my mother for supporting me in every way possible, including making breakfast for me every day to

the occasional drives to pick me up from school at 4 o'clock in the morning. Lana, my older sister, is, at times, a role model to me and, at times, my best friend. Thanks to you and to the newest member of the family, my brother-in-law Joohyung Oh, for letting me sleep over whenever I finished late. Thank you, Terry, my younger brother, for staying sweet and weird. Despite our lack of conversation, I know how much you supported me at heart.

Thank you, all of you, for your love and encouragement. I feel one step closer to saving the world. ☺